The Astrophysical Journal, 793:26 (17pp), 2014 September 20 doi:10.1088/0004-637X/793/1/26

THE VARIABLE HARD X-RAY EMISSION OF NGC 4945 AS OBSERVED BY *NUSTAR*

Simonetta Puccetti[1,2], Andrea Comastri[3], Fabrizio Fiore[2], Patricia Arévalo[4], Guido Risaliti[5,6], Franz E. Bauer[4,7], William N. Brandt[8,9], Daniel Stern[10], Fiona A. Harrison[11], David M. Alexander[12], Steve E. Boggs[13], Finn E. Christensen[14], William W. Craig[13,15], Poshak Gandhi[12], Charles J. Hailey[16], Michael J. Koss[17], George B. Lansbury[12], Bin Luo[8,9], Greg M. Madejski[18], Giorgio Matt[19], Dominic J. Walton[11], and Will Zhang[20]
[1] ASDC–ASI, Via del Politecnico, I-00133 Roma, Italy
[2] INAF–Osservatorio Astronomico di Roma, via Frascati 33, I-00040 Monte Porzio Catone (RM), Italy
[3] INAF–Osservatorio Astronomico di Bologna, via Ranzani 1, I-40127 Bologna, Italy
[4] Instituto de Astrofísica, Facultad de Física, Pontificia Universidad Católica de Chile, 306, Santiago 22, Chile
[5] INAF–Osservatorio Astrofisico di Arcetri, Largo E. Fermi 5, I-50125 Firenze, Italy
[6] Harvard–Smithsonian Center for Astrophysics, 60 Garden Street, Cambridge, MA 02138, USA
[7] Space Science Institute, 4750 Walnut Street, Suite 205, Boulder, CO 80301, USA
[8] Department of Astronomy and Astrophysics, The Pennsylvania State University, 525 Davey Lab, University Park, PA 16802, USA
[9] Institute for Gravitation and the Cosmos, The Pennsylvania State University, University Park, PA 16802, USA
[10] Jet Propulsion Laboratory, California Institute of Technology, 4800 Oak Grove Drive, Pasadena, CA 91109, USA
[11] Cahill Center for Astronomy and Astrophysics, California Institute of Technology, Pasadena, CA 91125, USA
[12] Department of Physics, Durham University, Durham DH1 3LE, UK
[13] Space Sciences Laboratory, University of California, Berkeley, CA 94720, USA
[14] DTU Space, National Space Institute, Technical University of Denmark, Elektrovej 327, 2800 Lyngby, Denmark
[15] Lawrence Livermore National Laboratory, Livermore, CA 945503, USA
[16] Columbia Astrophysics Laboratory, Columbia University, New York, NY 10027, USA
[17] Institute for Astronomy, Department of Physics, ETH Zurich, Wolfgang–Pauli–Strasse 27, CH–8093 Zurich, Switzerland
[18] Kavli Institute for Particle Astrophysics and Cosmology, SLAC National Accelerator Laboratory, Menlo Park, CA 94025, USA
[19] Dipartimento di Matematica e Fisica, Universit'a Roma Tre, via della Vasca Navale 84, I-00146 Roma, Italy
[20] NASA Goddard Space Flight Center, Greenbelt, MD 20771, USA
Received 2014 April 15; accepted 2014 July 14; published 2014 September 2

ABSTRACT

We present a broadband (∼0.5–79 keV) spectral and temporal analysis of multiple *NuSTAR* observations combined with archival *Suzaku* and *Chandra* data of NGC 4945, the brightest extragalactic source at 100 keV. We observe hard X-ray (>10 keV) flux and spectral variability, with flux variations of a factor of two on timescales of 20 ks. A variable primary continuum dominates the high-energy spectrum (>10 keV) in all states, while the reflected/scattered flux that dominates at $E < 10$ keV stays approximately constant. From modeling the complex reflection/transmission spectrum, we derive a Compton depth along the line of sight of $\tau_{\rm Thomson} \sim 2.9$, and a global covering factor for the circumnuclear gas of ∼0.15. This agrees with the constraints derived from the high-energy variability, which implies that most of the high-energy flux is transmitted rather than Compton-scattered. This demonstrates the effectiveness of spectral analysis at constraining the geometric properties of the circumnuclear gas, and validates similar methods used for analyzing the spectra of other bright, Compton-thick active galactic nuclei (AGNs). The lower limits on the *e*-folding energy are between 200 and 300 keV, consistent with previous *BeppoSAX*, *Suzaku*, and *Swift* Burst Alert Telescope observations. The accretion rate, estimated from the X-ray luminosity and assuming a bolometric correction typical of type 2 AGN, is in the range ∼0.1–0.3 $\lambda_{\rm Edd}$ depending on the flux state. The substantial observed X-ray luminosity variability of NGC 4945 implies that large errors can arise from using single-epoch X-ray data to derive $L/L_{\rm Edd}$ values for obscured AGNs.

Key words: galaxies: active – galaxies: individual (NGC 4945) – X-rays: galaxies

Online-only material: color figures

1. INTRODUCTION

The almost edge-on spiral starburst galaxy, NGC 4945, hosts one of the nearest active galactic nuclei (AGNs; $D \sim 3.8$ Mpc, see, e.g., Mouhcine et al. 2005; Mould & Sakai 2008; Tully et al. 2008; Jacobs et al. 2009; Tully et al. 2009; Nasonova et al. 2011). It has been the subject of many observations spanning a broad X-ray band, from sub-keV to hundreds of keV energies. X-ray emission from the infrared galaxy, NGC 4945, was discovered by *Ginga* and identified as a deeply buried AGN (Iwasawa et al. 1993). It is the brightest Seyfert 2 galaxy in the very hard (∼50–100 keV) X-ray sky, with a 10–50 keV flux of the order of 10^{-10} erg cm^{-2} s^{-1}, as seen by the *Compton Gamma-ray Observatory* (Done et al. 1996), the *Rossi Timing X-ray Explorer* (Madejski et al. 2000) and the PDS instrument on board *BeppoSAX* (Guainazzi et al. 2000).

The broadband spectrum, using high-energy data extending up to 100 keV in conjunction with softer X-ray observations from *ASCA* and *Ginga*, is described by a power-law continuum with strong photoelectric absorption (i.e., Done et al. 1996), with a column density, $N_{\rm H}$ (under the assumption of Solar abundances) of about 4×10^{24} cm^{-2}. This column and the observed high-energy variability identify NGC 4945 as a transmission-dominated Compton-thick AGN. In such sources, the high-energy ($E > 10$ keV) primary continuum penetrates the obscuring matter and peaks at 15–20 keV, depending on the actual value of the optical depth. Compton-thick AGNs are predicted to provide a significant contribution (from 10% to 30%, depending on the specific model assumptions) to the cosmic X-ray background spectrum at energies close to its ∼20–30 keV peak (Gilli et al. 2007; Treister et al. 2009). The X-ray spectrum of NGC 4945 also shows a strong iron K_α line

(EW >1 keV) that is thought to arise from fluorescence in matter, which is more remote from the nucleus than the primary continuum (e.g., Matt et al. 1996).

The hard X-ray emission in the *BeppoSAX* 15–200 keV band has been observed to vary by a factor of two on timescales as short as 10^4 s (Guainazzi et al. 2000). This suggests that the solid angle subtended by the Compton-thick absorber, as seen by the source, is unlikely to be large, and the heavy absorption of the primary continuum is probably confined to a disk-like structure or a "skinny" torus with a relatively small half-opening angle (<10°); otherwise, the scattered X-rays would noticeably dilute the hard X-ray variability (Madejski et al. 2000). NGC 4945 was also observed with *Suzaku* (Itoh et al. 2008), which confirmed the strong hard X-ray variability of the heavily obscured primary continuum. The spectrum below 10 keV is dominated by a constant reflected continuum along with neutral iron K_α, K_β, and nickel K_α lines. An extensive discussion of the origin of the hard X-ray emission from NGC 4945 is presented in Yaqoob (2012) using state-of-the-art Monte Carlo simulations (the MYTORUS model) to treat absorption and scattering in the Compton-thick regime. They conclude, in agreement with previous studies, though on much more solid statistical and physical grounds, that a clumpy medium with a small covering factor provides the best description of the observed spectrum and variability.

NGC 4945 has been observed by many instruments in the ∼0.5–10 keV band, and all data obtained so far indicate that it is almost constant in this energy range. High angular resolution observations with *Chandra* (Schurch et al. 2002; Done et al. 2003) reveal a clear change in the nature of the ∼0.5–7 keV X-ray spectrum with distance from the nucleus. The compact, unresolved emission confirms the basic absorbed power-law scenario given above. The closest (<50–100 pc) soft X-ray (∼0.5–5 keV) emission is likely associated with strong circumnuclear starburst activity that is well-modeled by a two-temperature (∼0.9 and ∼6 keV) optically thin thermal plasma (Schurch et al. 2002). The starburst region also contains cold reflection signatures (see also Marinucci et al. 2012). Despite the fact that the X-ray images in the line emission band (6.2–6.7 keV) and in the 2–7 keV band show an asymmetric and clumpy spatial distribution with a size of tens of parsecs, they almost perfectly match and are likely to be associated with the cold reflector. Unresolved clumpiness may explain the low covering factor inferred from the hard X-ray variability. The more distant region (beyond ∼50–100 pc) reveals distinctly different emission, with the spectrum showing soft continuum plus emission lines. This more extended emission appears morphologically as a plume, and was modeled as a combination of photoionized and collisionally ionized plasma, with $kT \sim 0.7$ keV (see Done et al. 2003 for details). The galaxy also contains off-nuclear variable ULXs (e.g., Brandt et al. 1996; Swartz et al. 2004; Isobe et al. 2008; Walton et al. 2011).

The nucleus of NGC 4945 is a strong source of megamaser activity, detected in H_2O (Dos Santos & Lepine 1979). Detailed, velocity-resolved maps reveal multiple megamaser spots revolving around the central black hole: this allows the precise determination of the black hole mass, at $1.4 \times 10^6\ M_\odot$ (Greenhill et al. 1997). The megamaser spots are irregularly distributed and clumpy.

Madejski et al. (2000) and Done et al. (2003) suggested that the megamaser spots are aligned with the absorbing disk/torus at 0.1–1 pc. In addition to this dense absorbing disk, the nucleus is completely embedded in a column of $\sim 10^{23}$ cm^{-2} at ∼25 pc, which may be due to a bar-driven gas inflow (Ott et al. 2001) or perhaps a high-latitude extension of the disk/torus. The extreme absorption region is surrounded by an extended, dusty, lower absorption region on scales of 50–100 pc in the starburst region.

The nucleus of NGC 4945 is characterized by a high and variable accretion rate. The Eddington ratio ($\lambda_{\rm Edd} = L_{\rm BOL}/L_{\rm EDD}$) is reported to be in the range of 0.1–0.5 (Guainazzi et al. 2000; Madejski et al. 2000; Done et al. 2003; Itoh et al. 2008). Yaqoob (2012) reported values as high as $\lambda_{\rm Edd} \simeq 2$. It is, however, important to note that super Eddington accretion rates are obtained assuming a distance of about 8 Mpc, which is about twice the distance commonly adopted for NGC 4945 ($D \sim 3.8$ Mpc).

NGC 4945 is the only known Compton-thick Seyfert 2 galaxy in the nearby universe (i.e., $z < 0.004$) that shows rapid variability in the very hard >10 keV X-rays. A detailed state-resolved spectral analysis with a very short time binning, which could not be performed with previous hard X-ray data, is the main scientific focus of the medium-deep monitoring *NuSTAR* observations described in this paper.

In Section 2, we describe the *NuSTAR* observations and archival observations. In Sections 3 and 4, we detail the variability properties. Section 5 presents the state-resolved spectral analysis. The results are discussed in Section 6 and the conclusions comprise Section 7.

Through out this paper, we adopt a NGC 4945 distance of 3.8 Mpc.

2. X-RAY OBSERVATIONS AND DATA REDUCTION

2.1. NuSTAR

We analyzed three *NuSTAR* observations of NGC 4945 performed in 2013 February, June, and July with the two focal plane modules A (FPMA) and B (FPMB; Harrison et al. 2013), for a total exposure time of ∼150 ks. Table 1 gives a log of the *NuSTAR* observations.

The telemetry raw fits files were processed using the *NuSTAR* Data Analysis Software package version 1.3.1 (NuSTARDAS; Perri et al. 2013). Calibrated and cleaned event files were produced using the calibration files in the *NuSTAR* CALDB (20131223) and standard filtering criteria with the *nupipeline* task. For the July observation, we followed a different procedure because portions of the observation had the raw positions of the laser spots outside of the calibrated range of the position sensing detector (see Harrison et al. 2013). Therefore, those data would be not be linearized using the standard calibration metrology grid file (see Perri et al. 2013). As a consequence, the sky position of the X-ray photons would be not calculated by the standard pipeline setting and these time intervals would be excluded from the calibrated and cleaned data. However, for the analysis of bright sources, the lost exposure time can be recovered by using the raw coordinates of the laser spots without applying the calibration correction; this is done at the expense of some positional uncertainty.

We applied this nonstandard analysis to the July observation; the reliability of the reconstruction of the sky coordinates was tested by comparing the two source brightness profiles generated using the cleaned event file produced with the standard and nonstandard analysis. We verified that the two profiles were fully consistent (99.9%, see Figure 1). Moreover, looking at the difference between the two brightness profiles, most of the photons are caught in the source extraction region (radius of 75″, see below). Therefore, we safely used the calibrated and cleaned data generated following the nonstandard analysis.

Table 1
NuSTAR NGC 4945 Observation Log

Observation ID[a]	RA_PNT[b] (deg.)	DEC_PNT[c] (deg.)	Exposure[d] (ksec)	Start Date[e]	Rate[f] (cts s^{-1})	Background[g]
60002051002	196.406	−49.4605	45.1	2013 Feb 10 T22:31:07	0.462 ± 0.002	3.9%
60002051004	196.3271	−49.461	54.5	2013 June 15 T04:56:07	0.519 ± 0.002	3.3%
60002051006	196.3334	−49.4907	50.5	2013 July 5 T22:51:07	0.349 ± 0.002	5.9%

Notes.
[a] Observation identification number.
[b] Right ascension of the pointing.
[c] Declination of the pointing.
[d] Total net exposure time.
[e] Start date and time of the observation.
[f] Mean value of the net count rate in the circular source extraction region with 75″ radius in the energy range 3–79 keV.
[g] Background percentage in the circular source extraction region with 75″ radius and in the energy range 3–79 keV.

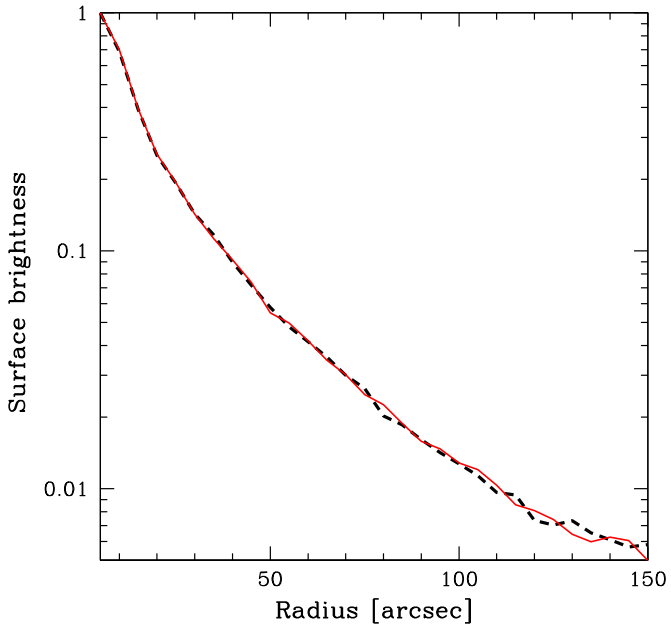

Figure 1. 3–79 keV source brightness profiles for the July observation. The red solid profile is the result obtained using the cleaned event file produced with the standard analysis; the black dashed profile is the result of the nonstandard analysis.

(A color version of this figure is available in the online journal.)

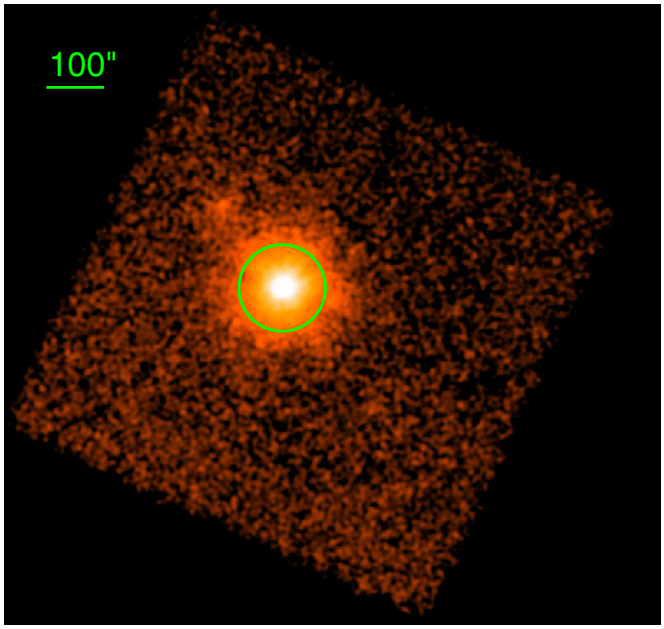

Figure 2. 3–79 keV *NuSTAR* image for the June observation and FPMA module. The image was smoothed with a Gaussian filter with $\sigma = 1.5$. The green circle is centered on the peak of the emission and has a radius of 75″.

(A color version of this figure is available in the online journal.)

We extracted the *NuSTAR* source and background spectra using the *nuproducts* task included in the NuSTARDAS package using the appropriate response and ancillary files. We extracted spectra and light curves in each focal plane module (FPMA and FPMB) using circular apertures of radius 75″ centered on the peak of the emission in the 3–79 keV data (see Figure 2). This choice maximizes the signal-to-noise ratio (S/N) of the data. Background spectra were extracted using source-free regions on the same detectors where the source is detected. As shown in Tables 1 and 4, the background count rates are a low fraction (<10%) of the source count rates for most observations in most energy intervals.

The large number of counts in the *NuSTAR* NGC 4945 spectra allows statistical grouping to oversample the instrument resolution. However, this can cause problems during spectral fitting because the bins are not completely independent. For this reason, the spectra were binned according to two criteria: (1) following the energy resolution multiplied by a factor of ∼0.4 at all energies, when possible; (2) to have an S/N > 4.5.

For the spectral analysis, in all cases, we co-added the spectra of each focal plane module into a single spectrum (e.g., for spectra at different time intervals), and we also combined the corresponding background spectra, response, and ancillary files. We used the *addascaspec* FTOOLS v.6.13, which combines spectra according to the method explained in the *ASCA* ABC guide.[21] The background normalization is calculated as for *ASCA* data.[22]

2.2. Chandra

The angular resolution of *NuSTAR* is dominated by the optics and has an 18″ FWHM with a half-power diameter of 58″ (Harrison et al. 2013). Therefore, *Chandra*, with its unsurpassed X-ray angular resolution (FWHM ∼ 0.″5), is an excellent complement to *NuSTAR* for analyzing the nucleus and nearby regions and for studying possible contamination from unresolved sources.

[21] http://heasarc.gsfc.nasa.gov/docs/asca/abc/
[22] http://heasarc.gsfc.nasa.gov/docs/asca/abc_backscal.html

Table 2
NGC 4945 Archival Data

Observatory	Observation ID[a]	Exposure[b] (ksec)	Start Date[c]	Ref[d]
BeppoSAX	50809001	40	1999 July 01 04:43:13.2	Guainazzi et al. 2000
Chandra ACIS-S	864	50	2000 Jan 27 19:00:10	Schurch et al. 2002
Chandra HETG ACIS–S	4899	79	2004 May 28 04:47:04	Marinucci et al. 2012
Chandra HETG ACIS–S	4900	97	2004 May 29 18:36:22	Marinucci et al. 2012
Suzaku	705047010	39	2010 July 04 15:15:58	Marinucci et al. 2012
Suzaku	705047020	44	2010 July 09 23:50:49	Marinucci et al. 2012
Suzaku	705047030	40	2010 July 26 01:36:35	Marinucci et al. 2012
Suzaku	705047040	39	2010 Aug 30 21:34:36	Marinucci et al. 2012
Suzaku	705047050	46	2011 Jan 29 02:05:50	Marinucci et al. 2012
Swift BAT	70 month catalog	7811[e]		Baumgartner et al. 2013

Notes.
[a] Observation identification number.
[b] Total net exposure time.
[c] Start date and time of the observation interval.
[d] Reference.
[e] On-axis equivalent exposure.

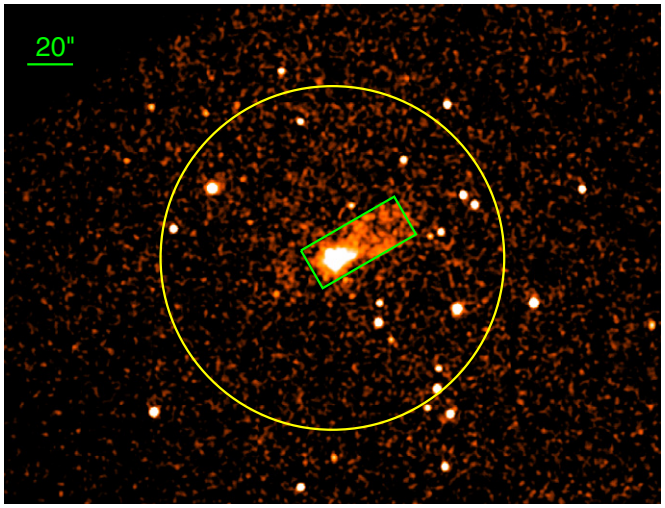

Figure 3. 0.5–7 keV image mosaic of the three *Chandra* observations (see Table 2). The green $47'' \times 19''$ box marks the region used to extract the *Chandra* spectra, which includes the nuclear source plus a spectrally soft, conically shaped X-ray plume (Schurch et al. 2002; Done et al. 2003). The yellow circle ($75''$ radius) marks the *NuSTAR* source extraction region.
(A color version of this figure is available in the online journal.)

We analyzed three archival *Chandra* observations collected in 2000–2004 (see Table 2) using the *Chandra* Interactive Analysis Observations (CIAO) software (v4.5; Fruscione et al. 2006) and the standard data reduction procedures. After cleaning for background flaring, the total exposures are ∼33 ks, ∼76 ks, and ∼97 ks for the 2000 and the two 2004 HETG-zeroth observations, respectively. The *specextract* task was used to extract the spectra; the 2004 spectra were combined using *addascaspec* from FTOOLS v.6.13, as described in Section 2.1. The spectra were binned to have at least 30 total counts per bin.

The *Chandra* spectra were extracted in a $47'' \times 19''$ box centered on R.A. = 13:05:26.331, Decl.= −49:27:56.41 (see Figure 3) to include the nuclear source plus a spectrally soft, conically shaped X-ray plume, due to starburst/superwind gas in a multiphase state, which extends $30''$ (∼500 pc) to the northwest (Schurch et al. 2002; Done et al. 2003) and is not resolved by *NuSTAR*.

Table 3
Chandra Serendipitous Source Contribution

Energy Range (keV)	Fac[a]	Fac[b]
0.5–2	82%	86%
2–3	85%	88%
3–4	74%	77%
4–5	69%	72%
5–6	47%	55%
6–7	18%	18%

Notes.
[a] The contribution of Chandra serendipitous sources to the NGC 4945 spectrum. The *NuSTAR* spectral extraction source region is a circle with $75''$ radius;
[b] Same as footnote [a] for the *Suzaku* spectral extraction source region (i.e., circle of $1.85'$ radius).

About 13 serendipitous point sources with S/N $\geqslant$ 3 in the 2–7 keV band are identified within the area corresponding to the *NuSTAR* extraction radius ($75''$) and about 20 sources are within the *Suzaku* spectral extraction region (see next section). By comparing the X-ray spectra of the nuclear region (including the plume), with the spectra of the serendipitous point sources, we estimate that the contamination by the nearby bright sources is of the order of ∼60% in the 4–6 keV energy band in both *NuSTAR* and *Suzaku* spectra (see Table 3). This evaluation is approximate and for guidance only. The serendipitous sources could be variable and their exact contribution depends on the energy range and detector point-spread function (PSF).

There is no evidence of any iron line emission in their spectra. The co-added spectrum of the five brightest "contaminants" is best-fitted by an absorbed power law ($\Gamma = 2.1\pm^{0.2}_{0.1}$, $N_{\rm H} = 1.1\pm^{0.4}_{0.3} \times 10^{22}$ cm^{-2}) plus a low-temperature thermal component ($kT = 0.22 \pm 0.07$ keV).

2.3. Suzaku

The energy resolution of *Suzaku* at ∼6 keV and the good counting statistics of the archival observations allow us to better constrain the spectral shape and the intensity of the iron line complex. Therefore, in the spectral analysis, we considered five

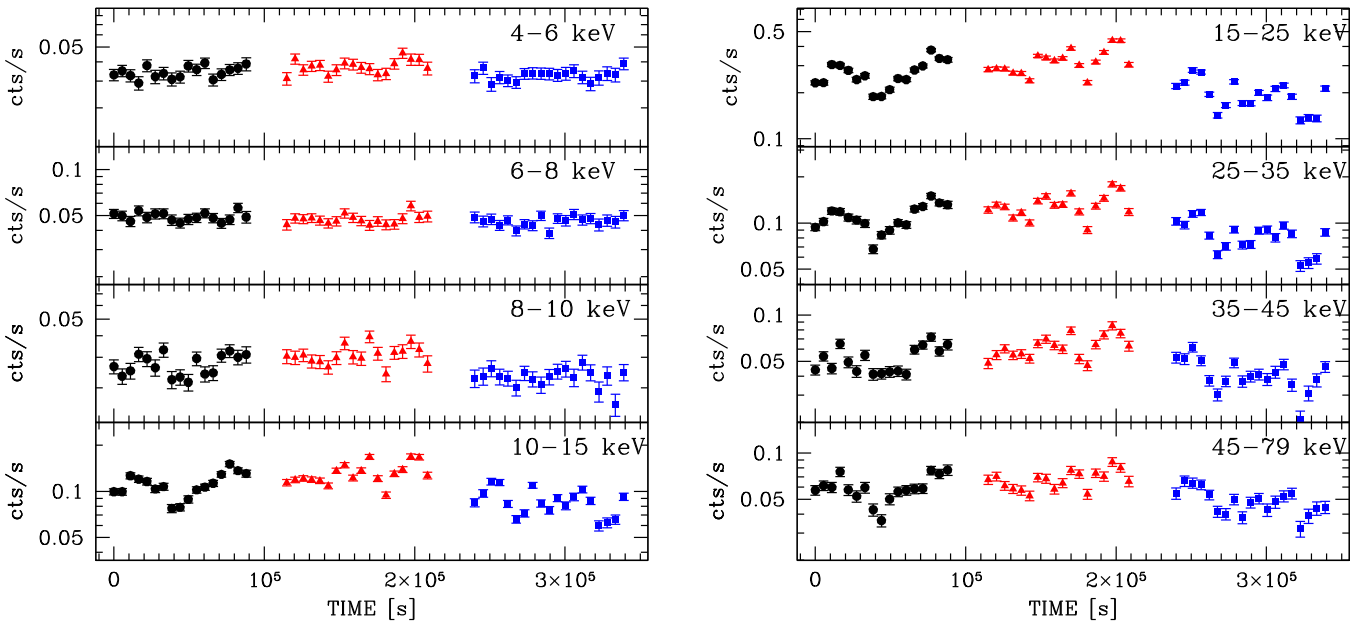

Figure 4. Light curves in bins of 5500 s (∼1 satellite orbit). The count rates are the mean values between those detected by the FPMA and FPMB modules, corrected for livetime, PSF losses and vignetting, but not for background. Left panel, from top to bottom: 4–6 keV, 6–8 keV, 8–10 keV, and 10–15 keV count rates. Right panel, from top to bottom: 15–25 keV, 25–35 keV, 35–45 keV, and 45–79 keV count rates. Black dots, red triangles, and blue squares refer to observations in February, June, and July, respectively. The real time interval between black dots and red triangles is about four months, whereas between red triangles and blue squares is about one month. The *y*-axis dynamic range is 0.9 in logarithmic scale, in each panel.

(A color version of this figure is available in the online journal.)

Suzaku observations performed between 2010 July and 2011 January (see Table 2). The X-ray imaging Spectrometer (XIS) data were extracted from a circular region with radius of 1.′85 (see Marinucci et al. 2012 for details on data reduction). The spectral cross-calibration between *NuSTAR* and *Suzaku* XIS is fairly good, with fluxes consistent within ∼10% (Walton et al. 2014; Brenneman et al. 2014).

The HXD-PIN data were reduced following the *Suzaku* data reduction guide (the ABC guide Version 5.0) using the rev2 data, which include all four cluster units. We used the instrumental background event file provided by the HXD-PIN team (NXB; Kokubun et al. 2007), which has a systematic uncertainty of ±(3–5)% (at the 1σ level). We extracted the source and background light curve in the same time interval, and corrected the source light curve for the detector dead time. The cleaned net exposure times were ∼32, 37, 32, 33, and 50 ks for the five *Suzaku* observations, respectively. The cosmic X-ray background spectrum was simulated using the spectral shape in Boldt (1987) and Gruber et al. (1999), and then added to the instrumental background, assuming a constant light curve.

The HXD-PIN count rate varies by a factor of ∼3.7 in the 16–80 keV energy range over the five observations.

2.4. BeppoSAX PDS

NGC 4945 was observed by *BeppoSAX* in 1999 (see Table 2). The PDS (Phoswitch Detector System, Frontera et al. 1997) data were calibrated and cleaned using the SAXDAS software with the standard method "fixed rise time threshold" for background rejection. PDS light curves are well-known to exhibit spikes on timescales between a fraction of a second to a few seconds and usually most counts from spikes are recorded below 30 keV. To screen the PDS data for such spikes, we followed the method suggested in the NFI user guide (Fiore et al. 1999). The PDS count rate light curve varies by a factor of ∼1.5 over a timescale of a few 10^4 s (see Guainazzi et al. 2000).

2.5. Swift BAT

We retrieve the *Swift* Burst Alert Telescope (BAT; Gehrels et al. 2004) NGC 4945 light curve and spectrum from the last public stack archive (see Table 2). The on-axis integration time is ∼7.81 Ms and the source has an S/N of ∼80 in the 14–195 keV energy range. The count rate uncertainty is fairly constant up to 100 keV; at higher energies the noise dominates. The BAT 14–195 count rate light curve varies by a factor of ∼3 over the 70 months.

3. *NUSTAR* LIGHT CURVES

The three *NuSTAR* observations span a timescale of ∼50 ks each (see Table 1). Figure 4 shows the *NuSTAR* light curves in bins of 5500 s (∼1 satellite orbit) in eight energy bands (4–6, 6–8, 8–10, 10–15, 15–25, 25–35, 35–45, and 45–79 keV); the light curves were corrected for livetime, PSF losses, vignetting, but not for background, which is negligible (see Table 4). Note that the *y*-axis dynamic range is the same in each panel of Figure 4.

We used the χ^2 test with a minimum confidence level of 2% to assess the variability of the light curves. We found that the 4–6 keV and 6–8 keV light curves are consistent with being constant and are not correlated with the other six energy bands. The 4–6 and 6–8 keV count rates are also constant among the three observations (taken within a time interval of ∼five months). The 8–10 keV light curves are consistent with being constant only in the July observation. The 8–10 keV variability pattern of the February and June observations correlates with all of the observing periods in the harder (>10 keV) bands. The 10–15, 15–25, 25–35, 35–45, and 45–79 keV light curves are not constant at a 99.9% confidence level, and are strongly correlated with each other in all the observations (see Figure 4 and the Spearman rank correlation coefficients in Table 4).

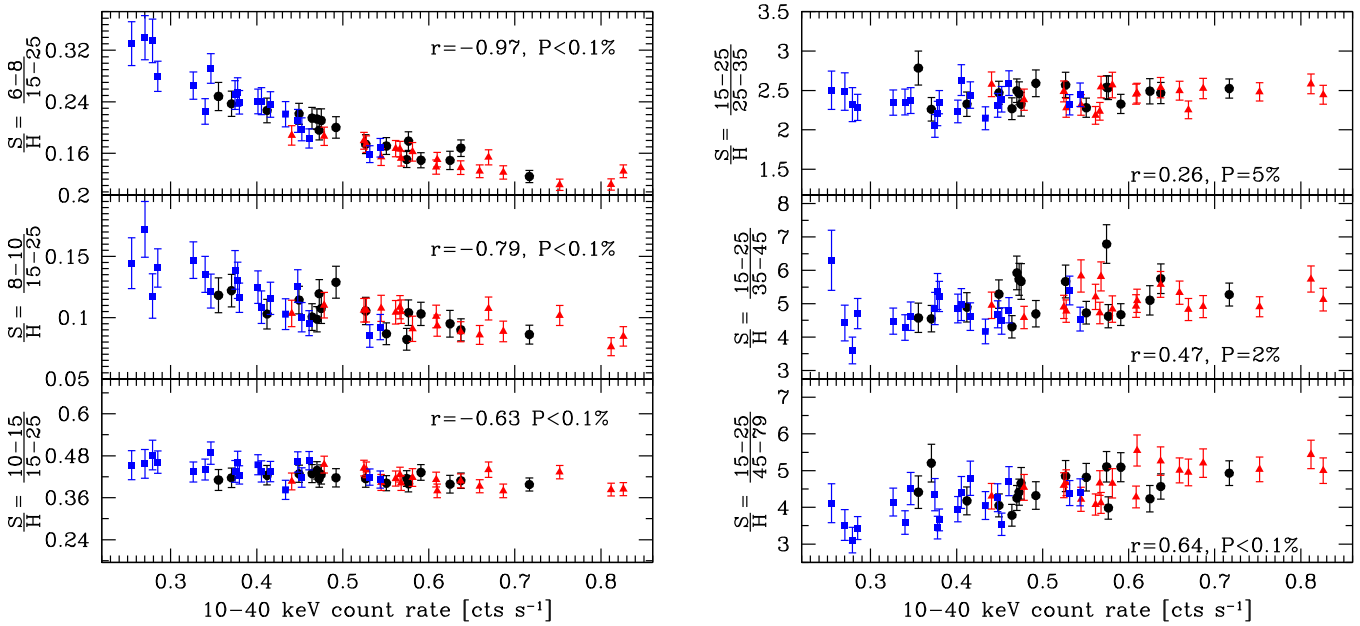

Figure 5. Hardness ratio vs. count rate in the 10–40 keV range. Black dots, red triangles, and blue squares have the same meaning as in Figure 4. The hardness ratio is evaluated by the relation S/H, where S and H are the count rates in two selected energy ranges, H being harder than S. Left panel: top (6–8)/(15–25); middle (8–10)/(15–25); bottom (10–15)/(15–25). Right panel: top (15–25)/(25–35); middle (15–25)/(35–45); bottom (15–25)/(45–79). Each panel shows the Spearman rank correlation coefficient, r, between the total hardness ratio and the count rate in the energy range 10–40 keV; P is the probability that the correlation is not statistically significant, evaluated by the Student's t test.

(A color version of this figure is available in the online journal.)

Table 4
Light Curve Mean Count Rate and Correlation Coefficient

Energy Range (keV)	Feb[a] (counts s^{-1})	Back_Feb[b]	Jun[c] (counts s^{-1})	Back_Jun[d]	Jul[e] (counts s^{-1})	Back_Jul[f]	r,P (Feb)[g]	r,P (Jun)[h]	r,P (Jul)[i]
4–6	0.034 ± 0.003	∼8%	0.037 ± 0.004	∼6.5%	0.033 ± 0.002	∼9%	0.17, 50%	0.53, 3%	0.04, >50%
6–8	0.049 ± 0.003	∼4%	0.047 ± 0.004	∼4%	0.046 ± 0.003	∼5%	0.14, >50%	0.38, > 10%	0.26, 20%
8–10	0.027 ± 0.004	∼6%	0.031 ± 0.004	∼4%	0.023 ± 0.003	∼7%	0.75, <0.1%	0.77, <0.1%	0.44, 5%
10–15	0.11 ± 0.02	∼2.5%	0.13 ± 0.02	∼2%	0.09 ± 0.02	∼3%	0.98, <0.1%	0.96, <0.1%	0.96, <0.1%
15–25	0.27 ± 0.05	∼1.5%	0.32 ± 0.06	∼1%	0.19 ± 0.04	∼2.5%	1, 0%	1, 0%	1, 0%
25–35	0.11 ± 0.02	∼4.5%	0.13 ± 0.02	∼4%	0.08 ± 0.02	∼6.5%	0.95, <0.1%	0.94, <0.1%	0.94, <0.1%
35–45	0.05 ± 0.01	∼5%	0.06 ± 0.01	∼4%	0.04 ± 0.01	∼8%	0.82, <0.1%	0.91, <0.1%	0.89, <0.1%
45–79	0.06 ± 0.01	∼13%	0.07 ± 0.01	∼12%	0.05 ± 0.01	∼19%	0.84, <0.1%	0.77, <0.1%	0.81, <0.1%

Notes.
[a] Mean values of the light curve count rates for the 2013 February observation, in the energy range indicated in the first column of the table.
[b] Background percentage in the circular source extraction region with 75″ radius.
[c] Same as [a] for the 2013 June observation.
[d] Same as [b] for the 2013 June observation.
[e] Same as [a] for the 2013 July observation.
[f] Same as [b] for the 2013 July observation.
[g] r is the Spearman rank correlation coefficient between the light curves of the 2013 February observation, in the energy range indicated in the first column of the table and the energy range 15–25 keV; P is the probability that the correlation is not statistically significant, evaluated by the Student's t test.
[h] Same as [g] for the 2013 June observation.
[i] Same as [g] for the 2013 July observation. The quoted errors are at the 90% confidence level for one parameter of interest.

At energies <8 keV the light curves are approximately constant, while at energies >10 keV the variability pattern is roughly self-similar up to energies of the order of 45 keV. Therefore, to investigate possible spectral changes, the count rates in the 10–40 keV band were considered. This energy range represents the best trade-off between counting statistics and variability pattern. The hardness ratios versus the 10–40 keV count rates are shown in Figure 5. The largest amplitude variability (a factor of 3.3) is observed in the 6–8 keV versus 15–25 keV ratio. Significant variability is also observed in the (15–25)/(35–45) and (15–25)/(45–79) ratios, while the spectral shape in the ∼15–35 keV region is similar for the three observations and is independent of the 10–40 keV count rate.

The *NuSTAR* 10–40 keV count rate varies by almost a factor of four over the three observing periods, and by factors of up to ∼1.5 on timescales as short as ∼2900 s with doubling/halving timescales of the order of ∼16 ks (see Figure 6).

The constant count rate level of the 6–8 keV light curve, which includes a strong iron line emission (see Yaqoob 2012, and references therein), suggests a constant contribution by the reflection continuum emission, if most of the iron line emission

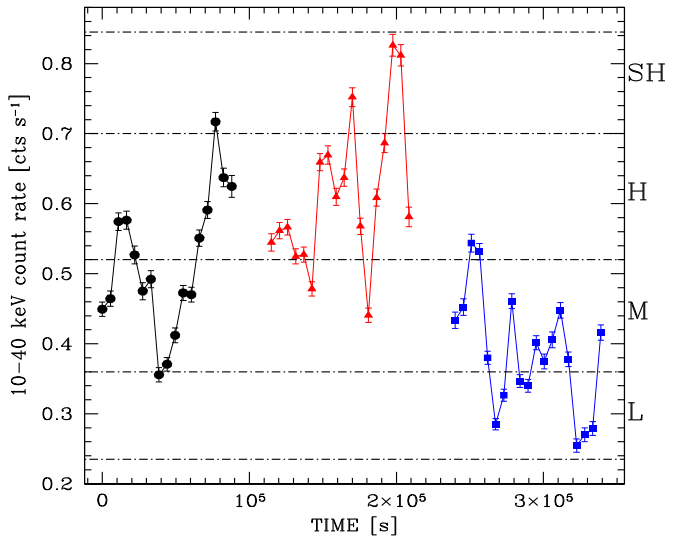

Figure 6. Count-rate light curves in the 10–40 keV energy range, in bins of 5500 s (∼1 satellite orbit). The symbols are the same as in Figure 4. The light curves are divided into four count-rate ranges, marked by the dot-dashed lines and capital letters on the right (see Section 5.1).

(A color version of this figure is available in the online journal.)

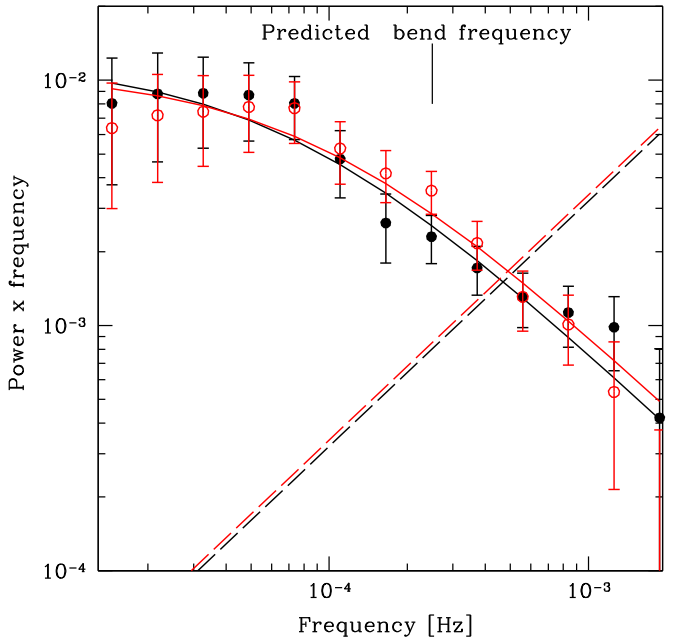

Figure 7. Power density spectra in the 10–79 keV band for FPMA (black filled circles) and FPMB (red open circles). The error bars represent only the stochastic nature of red-noise light curves. The solid lines represent the best-fitting models for each focal plane module. The dashed lines represent the Poisson noise level for each focal plane module, which has been subtracted from the power density spectra. In the plot, the constant Poisson noise appears as a linearly increasing function and the −1 slope of the low-frequency power spectrum appears horizontal.

(A color version of this figure is available in the online journal.)

originates from the same cold reflector (see Marinucci et al. 2012).

The hardness ratio analysis may provide valuable hints on the spectral components responsible for the observed variability. The 10–40 keV count rate is strongly anticorrelated with the (6–8)/(15–25) ratio, and exhibits a slighter anticorrelation with the (8–10)/(15–25) and (10–15)/(15–25) ratios. This behavior and the constant count rate level of the 6–8 keV light curves suggest variations of the flux level of the primary emission and/or of the column density of the obscuring circumunclear material. On the other hand, the correlation between the 10–40 keV flux and the (15–25)/(35–45) and (15–25)/(45–79) ratios suggests that the photon index of the power law steepens while the 10–40 keV count rates increases.

The spectral variability is investigated in detail by means of count rate resolved spectral analysis as described in Section 5.

4. *NUSTAR* POWER DENSITY SPECTRUM

We produced background-subtracted light curves in the 10–79 keV band for each observation, with FPMA and FPMB analyzed separately (see Section 3). We calculated the power spectrum for each focal plane module, combining the three observations, using the method described in Arévalo et al. (2012). Since each observation covers a timescale of about 10^5 s and gaps between the observations are orders of magnitude longer, only frequencies above 10^{-5} Hz are effectively probed.

The Poisson noise produced by the finite number of counts in each time bin introduces additional white noise variability in the light curves. This Poisson noise therefore adds a constant amount of power to each frequency bin in the power spectra. We estimated the average Poisson noise power from the high-frequency end of each power spectrum, obtaining a value within 10% of a simple estimate based on the light curve errors. This average Poisson power was then subtracted and the resulting power spectra and the Poisson noise are shown in Figure 7. Since the two focal plane modules function simultaneously, the two power spectra represent the same intrinsic variations in the flux and only differ due to the effects of Poisson noise. The largest differences are around timescales of a few thousand seconds, which corresponds to the orbital gaps. These timescales are less well sampled and more uncertain.

The power spectra are dominated by Poisson noise only at the highest frequencies, above 10^{-3} Hz. Below this frequency, the power spectra rise steeply, following an approximate power-law behavior.

We fitted each power spectrum with a bending power-law model $P(f) = Af^{\alpha_L}\ [1 + (f/f_b)^{(\alpha_L-\alpha_H)}]^{-1}$, as normally used for lower energy X-ray power spectra of AGNs (see McHardy et al. 2006, and references therein). We obtained good fits (χ^2 probability ∼2.5% and ∼10%, for FPMA and FPMB) fixing the low-frequency slope α_L at −1, the high-frequency slope α_H at −2, and allowing the bend frequency and normalization to vary. The best-fitting models for each focal plane module are shown in Figure 7. The bend frequency 90% error bands for two parameters of interest are 2.8×10^{-5}–2.0×10^{-4} Hz for FPMA and 4.5×10^{-5}–1.8×10^{-4} Hz for FPMB; as expected, the simultaneous observations produce consistent power spectrum parameters. These results are marginally consistent with the *RXTE* findings (Mueller et al. 2004).

In unobscured AGNs, the power density spectrum bend frequency scales with black hole mass and accretion rate as

$$\log T_B = 2.1 \log M_{\odot,6} - 0.98 \log L_{\rm bol,44} - 2.28, \quad (1)$$

where T_B is the break timescale in days, $M_{\odot,6}$ is the black hole mass in units of $10^6\ M_\odot$, and $L_{\rm bol,44}$ is the bolometric luminosity in units of 10^{44} erg s^{-1} (see McHardy et al. 2006).

Using a black hole mass of $1.4 \times 10^6\ M_\odot$ (Greenhill et al. 1997) and a nuclear luminosity of $L_{\rm bol} = 0.1\ L_{\rm Edd}$ (Madejski et al. 2000; Guainazzi et al. 2000), relation (1) predicts a

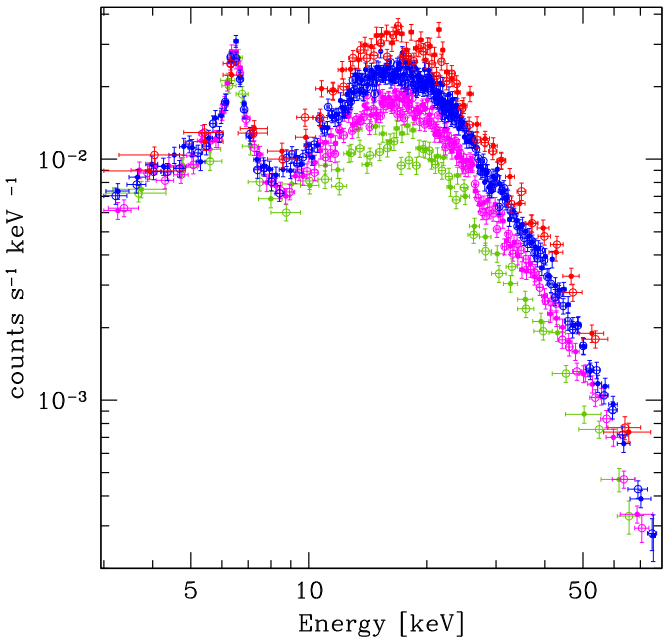

Figure 8. *NuSTAR* spectra in the 3–79 keV energy range. The solid dots are FPMA data, and open dots are FPMB data. The colors represent: green—L state, magenta—M state, blue—H state and red—SH state.

(A color version of this figure is available in the online journal.)

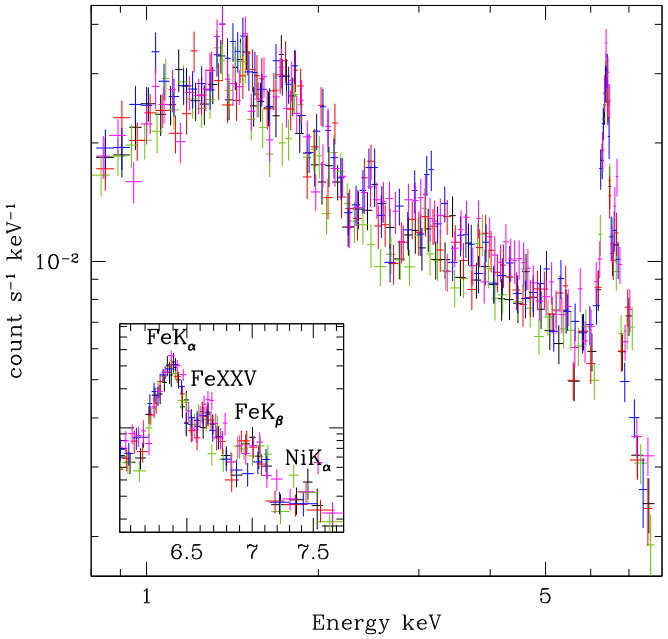

Figure 9. *Suzaku* XIS data in the 0.8–8 keV energy range. The colors represent the five observations (see Table 2). The inset panel shows a zoom of the iron complex (i.e., FeK_α, FeK_β, and Compton shoulder, Fe xxv) and the nickel emission line.

(A color version of this figure is available in the online journal.)

bend timescale of $T_B = 0.05$ days, corresponding to a bend frequency of $f_B = 2.3 \times 10^{-4}$ Hz. This is larger than our best-fit value in the 10–79 keV band ($\sim 1 \times 10^{-4}$ Hz). Nevertheless, considering the bend frequency 90% uncertainties and the intrinsic scatter in the compilation of data that leads to the relation in McHardy et al. (2006), we conclude that the measured power density spectrum of NGC 4945 is in good agreement with the behavior of the power-law continuum in unobscured sources.

An attempt to build power density spectra for the four individual states obtained by dividing the *NuSTAR* light curves into four count rate ranges (see Figure 6 and Section 5) was limited due to the short time interval of each state and the stochastic nature of the variability. The power density spectra of each state are consistent and no clear trend can be detected between flux level and power density spectral shape or normalization. Therefore, the various observations are consistent with arising from the same variability mechanism.

5. STATE-RESOLVED SPECTRAL ANALYSIS

5.1. The Spectra

Given that the spectral shape depends on the ∼10–40 keV count rate, as seen in Figure 5, and the 10–40 keV count rate varies by almost a factor of four over the three observing periods, we characterize the spectral variability with a proper spectral analysis where four states were considered. The corresponding time intervals were chosen as a trade off between a relatively high counting statistic for the spectral analysis and a relatively short time interval to limit rapid variability.

We divided the observations into intervals corresponding to four count rates in the 10–40 keV band. As shown in Figure 6, we refer to these count-rate intervals as the low (L), medium (M), high (H), and super-high (SH) states. The four corresponding *NuSTAR* spectra, shown in Figure 8, have exposure times of ∼21 ks, ∼55 ks, ∼63 ks and ∼11 ks, respectively.

Previous X-ray observations have clearly shown that the broad (∼0.5–200 keV) spectrum of NGC 4945 is complex, requiring a relatively large number of spectral components (see Yaqoob 2012; Marinucci et al. 2012, and references therein). Moreover, the *NuSTAR* spectra are extracted from spatial regions that encompass unrelated contaminating sources and extended emission.

We made use of the excellent spatial resolution of the *Chandra* observations to model the soft thermal emission due to the starburst/X-ray plume and point-like contaminating sources, and the good spectral resolution of *Suzaku* to enhance the studies of the iron line complex at 6–7 keV. Given that the X-ray emission of NGC 4945 below 10 keV is relatively constant (within 10%; see Marinucci et al. 2012, see also Figure 9) and consistent with the *NuSTAR* light curves below ∼8 keV, we performed simultaneous fits of the *NuSTAR*, *Suzaku* XIS, and *Chandra* data, following the method described below (see Figure 12). The spectral analysis for the four states (L, M, H, and SH) was performed with XSPEC (Arnaud 1996) v12.8.0.

In order to obtain a hint of the components that dominate the observed spectral variability, we computed the difference spectrum between the highest (SH) and lowest (L) count rate states. The resulting spectrum (Figure 10), resembling a heavily absorbed power law, has statistically significant counts in the ∼8–79 keV energy range. The difference spectrum is best fitted with an absorbed power law (PLCABS; Yaqoob 1997) $\Gamma \sim 1.9 \pm 0.1$ and $N_{\rm H} \sim 4.2 \pm 0.2 \times 10^{24}$ cm^{-2}. Given the good agreement between the best-fit values of the difference spectrum and those obtained from the state resolved analysis using the same model (see Section 5.4), it is tempting to conclude that the observed variability pattern is mostly due to variations of the primary continuum. In order to further investigate the origin of the variability, we made the following test. The SH state is fitted by varying a few parameters, whose initial values were determined by the L state fit. The free parameters are the

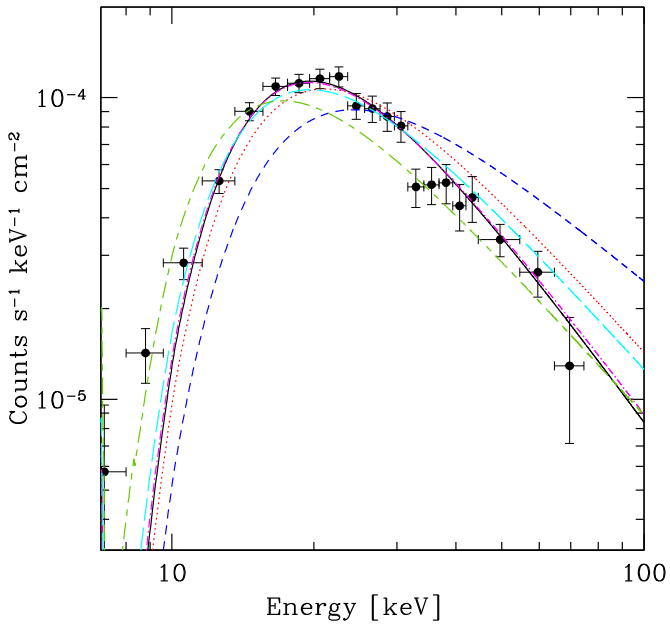

Figure 10. Spectrum obtained by subtracting the L state spectrum from the SH state spectrum (black solid points). The lines show the best-fit model allowing variations of: (a) normalization of the primary continuum (red dotted line); (b) photon index of the primary continuum (blue short dashed line); (c) absorbing column density of the primary continuum (olive short dashed–long dashed); (d) normalization and photon index of the primary continuum (black solid line); (e) normalization and absorbing column density of the primary continuum (cyan long-dashed line); (f) normalization, photon index, and absorbing column density of the primary continuum (magenta dotted-short dashed).

(A color version of this figure is available in the online journal.)

normalization and the photon index of the primary continuum, the absorbing column density, and any meaningful combination of them.

Using a χ^2 test with a minimum confidence level of 2%, the best-fit for the residual spectrum is obtained for variations of the order of a factor of ∼6–8 for the normalization and $\Delta\Gamma \sim 0.2$–0.3 for the slope of the primary continuum (see Figure 10). The quality of the fit slightly improves ($\Delta\chi^2 \simeq 2$ for $\Delta\mathrm{dof} = 1$) when a variation of the column density is included ($\Delta N_{\rm H} \sim 0.1$–$0.2 \times 10^{24}$ cm^{-2}). We conclude that most of the observed variability has to be ascribed by the intensity of the primary continuum flux and, to a lower extent, to a steepening of the power-law slope from the low to the super-high state. If the variability were mainly driven by absorbing column density variations, these should be of the order of $\Delta N_{\rm H} \sim 1.5 \times 10^{24}$ cm^{-2}, and would have been easily recognized by this preliminary analysis.

5.2. The Model

Due to the wealth of data obtained by previous observations, the main components contributing to the broadband X-ray emission of NGC 4945 are relatively well-established. Guided by the previous results, the broadband X-ray spectrum is modeled as follows.

1. An isotropic primary continuum modeled with a power law, modified by heavy photoelectric absorption and including Compton scattering effects (see, e.g., Yaqoob 2012).
2. A cold reflection component (see, e.g., Marinucci et al. 2012).
3. The iron complex (i.e., FeK_α at 6.4 keV, FeK_β at 7.06 keV and the Compton shoulder) and the nickel line at 7.47 keV detected through a simultaneous fit of the five XIS observations (see Figure 9 and, e.g., Itoh et al. 2008).
4. A multi-temperature thermal plasma to account for the nuclear and extended starburst region, where the hottest component includes the Fe XXV emission line at ∼6.66 keV (Schurch et al. 2002; Done et al. 2003).
5. An absorbed soft power law plus low temperature plasma ($kT \sim 0.2$ keV) to account for the contaminating sources as described in Section 2.2.

Preliminary fits of the five *Suzaku* XIS observations, including the contamination component (c), indicate that the FeK_α, Fe XXV, and FeK_β emission lines are statistically significant at a 99.99% confidence level according to the *F*-test, while the nickel line improves the fit at 99.95% confidence level.

The ionized material from which Fe XXV originates could be either predominantly plasma, collisionally heated by the starburst activity around the nucleus (Schurch et al. 2002; Done et al. 2003), or photoionized by the nucleus (Itoh et al. 2008; Yaqoob et al. 2012). In either case, it will contain free electrons that scatter a fraction of the nuclear light, producing a continuum with approximately the same shape as the incident AGN emission, i.e., a power law (Done et al. 2003; Bianchi et al. 2006).

Itoh et al. (2008), Yaqoob et al. (2012), and Marinucci et al. (2012) using *BeppoSAX* and/or *Suzaku* data, based their analysis on the photoionization case, including in their overall model a warm scattering power law, which is likely to include the contribution of serendipitous sources in the NGC 4945 field. From a spectral point of view, a warm scattered power law can be hardly distinguished from the summed spectrum of serendipitous contaminating sources.

Due to the *Chandra* high angular resolution, Done et al. (2003) found that the starburst rather than the photoionization scenario better describes the data, consistently with previous results (Schurch et al. 2002). They also found that any soft scattered component from the hot gas is negligible compared to its diffuse emission (i.e., a factor of $\sim 10^5$ smaller than the primary continuum). Moreover, at low X-ray energies, the recombination lines expected in the photoionization scenario are not detected in the NGC 4945 reflection grating spectrometer (RGS on board *XMM-Newton*; Guainazzi & Bianchi 2007). For these reasons, we believe that the soft X-ray spectrum of NGC 4945 is best described by thermal emission from a hot plasma due to starburst activity, which is commonly observed in starburst galaxies (e.g., NGC 253 Pietsch et al. 2001, NGC 6240 Boller et al. 2003). As a consequence, a warm scattering power law is not considered any further.

All the spectral components are redshifted using $z = 0.001878$ (see, e.g., Mouhcine et al. 2005; Mould & Sakai 2008; Tully et al. 2008, 2009; Jacobs et al. 2009; Nasonova et al. 2011).

5.2.1. Primary Continuum, Cold Reflection, and Emission Lines: Model Components (a), (b), and (c)

Fits were performed using the MYTORUS model[23] (Murphy & Yaqoob 2009; Yaqoob & Murphy 2011). Spectral fits with reflection and transmission models previously used in the literature (PEXRAV and PLCABS) are briefly discussed for comparison purposes in Section 5.4.

Assuming that the direct continuum emission is a power law, three tables are needed to run spectral fits: MYTORUSZ (i.e., model component (a)), MYTORUSS (i.e., model component (b)), and MYTORUSL (i.e., model component (c)). The first is a

[23] http://www.mytorus.com/

multiplicative table that contains the pre-calculated transmission factors that distort the direct continuum at all energies owing to photoelectric absorption and Klein Nishina scattering (see Section 5.2 of the MYTORUS manual); MYTORUSS and MYTORUSL represent the scattered/reflected continuum toward the line of sight and the emission lines (i.e., FeK_α, FeK_β, and Compton shoulder), respectively. These line tables are made with a range of energy offsets for best-fitting the peak energies of the emission lines. Extensive testing showed that an offset of +10 eV is optimal for the NGC 4945 *NuSTAR*, *Suzaku*, and *Chandra* data. This covers both intercalibration instrumental energy offsets, and takes into account any residual offset due to a blend of neutral and mildly ionized iron.

MYTORUS does not include a cutoff energy, but allows different termination energies. The high-energy cutoff in NGC 4945 is almost completely unconstrained. Lower limits were reported on the basis of *Suzaku* (>80 keV) and *Swift* BAT (>100 keV) spectra by Itoh et al. (2008) and Yaqoob (2012), respectively. A reanalysis of *BeppoSAX* data suggests that the lower limit on the cutoff energy could be as high as 200 keV in agreement with previous findings (Guainazzi et al. 2000). Therefore, in the following, we used a termination energy of 500 keV, corresponding to no cutoff within the *NuSTAR* band. Tests were also made with a termination energy of 200 keV without noticeable differences.

The original geometry assumed in the Monte Carlo calculations to generate the MYTORUS tables is that of a uniform torus with a circular cross section; the diameter is characterized by the equatorial column density $N_{\rm H}$, and the opening angle with respect to the axis of the system is fixed to 60°, corresponding to a covering factor of 0.5.

In the case of NGC 4945 the high $\tau_{\rm Thomson}$[24] (two to three) and the rapid high-energy variability suggest that the absorber has a small effective global covering factor (∼0.1–0.2) and a different geometrical configuration with respect to the toroidal geometry (see, e.g., Madejski et al. 2000; Done et al. 2003; Yaqoob et al. 2012). For this reason, we run MYTORUS routines in a "decoupled" mode mimicking a clumpy absorber with an arbitrary effective global covering factor (see Yaqoob 2012 for more details). A few tests with MYTORUS in the standard configuration were performed for a comparison with previous results and are discussed in Section 5.4.

In the "decoupled" mode configuration the inclination angle between the observer's line of sight and the symmetry axis of the torus (hereafter $\theta_{\rm obs}$) is decoupled from the column density $N_{\rm H}$ intercepted by the direct continuum. In this case, the direct continuum is purely a line-of-sight quantity, independent of geometry, and the angle $\theta_{\rm obs}$ is fixed to 90°. In a patchy distribution of clouds in the background and/or from a uniform distribution with a favorable geometry, part of the reflection from the inner far side of the reprocessor could be unobscured by material on the near side of the obscuring material. In this case, the far-side reflection, at least below ∼10 keV, could dominate the observed spectrum. This back-reflected continuum and the associated lines are parameterized with a MYTORUS face-on reflection spectrum, obtained fixing $\theta_{\rm obs}$ to 0°. Instead, the forward scattered emission and associated emission lines are approximated using a MYTORUS edge-on reflection spectrum, obtained fixing $\theta_{\rm obs}$ to 90°.

In the most general case, the column density $N_{\rm H}$ obscuring the direct continuum can be decoupled from the column density responsible for the back-reflection, the forward-reflection, or both. As shown in Section 5.3, leaving the $N_{\rm H}$ associated with the various components free to vary does not improve the fit. Moreover the various column densities are consistent each other. A single $N_{\rm H}$ value is then adopted, consistently with Yaqoob (2012).

The XSPEC format is:

ZPOWERLW×MYTORUSZ($\theta_{\rm obs}$ = 90°)+MYTORUSS($\theta_{\rm obs}$ = 90°) GSMOOTH×MYTORUSL($\theta_{\rm obs}$ = 90°)+MYTORUSS($\theta_{\rm obs}$ = 0°)+ GSMOOTH×MYTORUSL($\theta_{\rm obs}$ = 0°)+ZGAUSS.

The zgauss component models the NiK_α line, which is not included in the MYTORUS emission lines. In the following, we refer to the normalization (i.e., photons keV^{-1} cm^{-2} s^{-1}) of the primary direct continuum, forward-scattered continuum, forward-scattered emission lines, back-scattered continuum, and back-scattered emission lines as A_{Z90}, A_{S90}, A_{L90}, A_{S0}, and A_{L0}, respectively. The normalization of the scattered (reflected) continua and the corresponding emission lines are linked together $A_{L90} = A_{S90}$ and $A_{L0} = A_{S0}$.

5.2.2. Multi-temperature Thermal Plasma: Model Component (d)

We jointly fit the three *Chandra* (0.5–8 keV) data sets using the best-fit parameters for the high-energy emission (components (a), (b), (c); Section 5.2.1) with an additional multi-temperature thermal plasma (component (d)). The photon index and the absorbing column density $N_{\rm H}$ of the continuum are fixed to the mean values evaluated by the spectral analysis described in the previous section ($\Gamma = 1.9$, $N_{\rm H} = 3.55 \times 10^{24}$ cm^{-2}).

Following Schurch et al. (2002), the soft thermal emission due to the starburst/X-ray plume is modeled with a three-temperature, optically thin thermal plasma, allowing the absorption of each component to vary independently. The XSPEC format for component (d) is:

CONSTANT×WABS_1×(MEKAL_1 + WABS_2×MEKAL_2 + WABS_3×MEKAL_3),

where the WABS_1 component is fixed to the Galactic column density and the constant is the normalization factor between the *Chandra* observation performed in 2000 and the two performed in 2004. The normalization factor is $1.00\pm^{0.07}_{0.05}$, confirming that the NGC 4945 X-ray emission below 10 keV is relatively constant. In the following the normalization is fixed to unity.

Our *Chandra* best-fit model (Figure 11 and Table 5) is fully consistent with previous results (Schurch et al. 2002; Done et al. 2003). Model component (d) in the final spectral analysis for the four states (L, M, H, and SH) is fixed to the *Chandra* best-fit parameters.

5.2.3. Contaminating Sources: Model Component (e)

The effect of contamination due to individual sources within the *NuSTAR* and *Suzaku* extraction regions is parameterized with an absorbed power law and low temperature plasma plus absorption (see Section 2.2). To this aim, the *NuSTAR* (3–79 keV), *Suzaku* XIS (0.8–7.8 keV), and *Chandra* ACIS (0.5–7.8 keV) data are jointly fitted using the spectral components (a), (b), (c), and (d), while component (e) is applied only to the *NuSTAR* and *Suzaku* data.

The mean values of the best-fitting parameters of the absorbed power law are: $\Gamma = 2.22 \pm 0.01$, $N_{\rm H} = (1.26 \pm 0.14) \times 10^{22}$ cm^{-2}, and a normalization at 1 keV of $(8.2 \pm 0.9) \times 10^{-4}$ photons keV^{-1} cm^{-2}s^{-1}. The corresponding values for the thermal component are: $kT = 0.17 \pm 0.01$ keV, $N_{\rm H} = (0.81 \pm 0.12) \times 10^{22}$ cm^{-2}, and normalization $(2.0 \pm 0.6) \times$

[24] $\tau_{\rm Thomson} = x \times \sigma_{\rm Thomson} \times N_{\rm H}$, where x is the mean number of electrons per H atom, which is ∼1.2 assuming cosmic abundance.

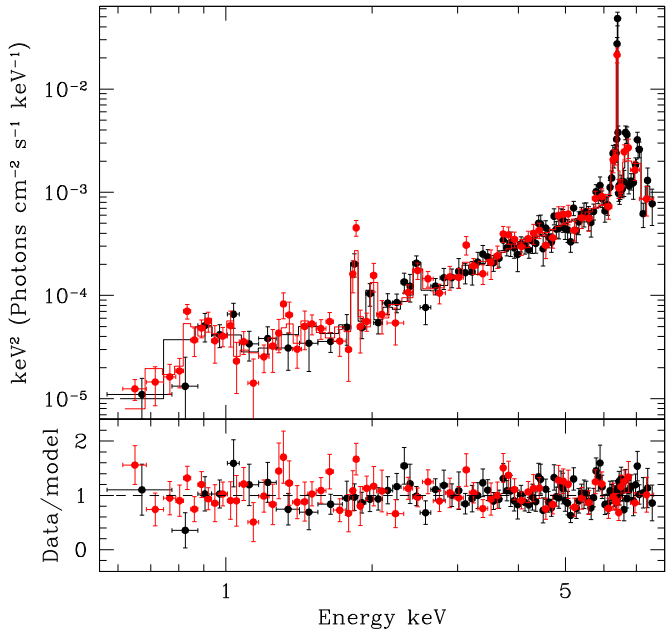

Figure 11. *Chandra* spectra, unfolded with the instrument response, of the NGC 4945 nucleus plus X-ray plume; with the two co-added 2004 observations performed by HETG (zeroth) shown in black and the 2000 observation performed by ACIS-S shown in red (see Table 2). The lower panel shows the data/model residuals.

(A color version of this figure is available in the online journal.)

Table 5
Multi-temperature Thermal Plasma: *Chandra* Best-fitting Parameters

Parameter	Value
N_{H1}[a]	0.157
kT_1[b]	$0.67\pm^{0.11}_{0.07}$
K_1[c]	$2.1\pm^{0.3}_{0.4}\times10^{-5}$
N_{H2}[a]	$2.0\pm^{0.6}_{0.4}$
kT_2[b]	$0.9\pm^{0.2}_{0.2}$
K_2[c]	$5.3\pm^{3.5}_{1.6}\times10^{-4}$
N_{H3}[a]	$10.5\pm^{4.9}_{3.3}$
kT_3[b]	$4.0\pm^{2}_{1.6}$
K_3[c]	$8\pm^{8}_{2}\times10^{-4}$
PHA bins	171
Degrees of freedom	160
χ^2	137.2

Notes. The table reports the *Chandra* best-fit values with uncertainties at the 90% confidence level for one parameter of interest ($\Delta\chi^2 = 2.706$) for the model component (d).
[a] Column density N_H in units of 10^{22} cm^{-2}. The first component, WABS_1, is fixed to Galactic column density (Heiles & Cleary 1979).
[b] Temperature in keV.
[c] Normalization at 1 keV in unit of photons keV^{-1} cm^{-2}s^{-1} for the spectral components. Subscripts refer to the spectral component number (see Section 5.2.2).

10^{-2} photons keV^{-1} cm^{-2}s^{-1}. The *NuSTAR* 4–10 keV flux of the component (e) is $\sim10^{-12}$ erg s^{-1} cm^{-2}. The *Suzaku* contamination flux is within ±10% of the *NuSTAR* one. In the final spectral analysis for the four states (L, M, H, and SH), the parameters of spectral component (e) are fixed to the best-fit values reported above.

Table 6
Best-fitting Parameters

Parameter	L	M	H	SH
Γ[a]	$1.77\pm^{0.09}_{0.09}$	$1.88\pm^{0.05}_{0.04}$	$1.95\pm^{0.03}_{0.04}$	$1.96\pm^{0.07}_{0.07}$
N_H[b]	$3.5\pm^{0.2}_{0.2}$	$3.6\pm^{0.1}_{0.1}$	$3.6\pm^{0.1}_{0.1}$	$3.5\pm^{0.1}_{0.1}$
A_{Z90}[c]	$0.21\pm^{0.11}_{0.07}$	$0.51\pm^{0.15}_{0.11}$	$0.98\pm^{0.20}_{0.17}$	$1.28\pm^{0.51}_{0.36}$
A_{S90}[d]	$\leqslant0.04$	$0.04\pm^{0.03}_{0.02}$	$0.06\pm^{0.03}_{0.03}$	$0.07\pm^{0.05}_{0.04}$
A_{S0}[e]	$0.009\pm^{0.002}_{0.002}$	$0.012\pm^{0.002}_{0.002}$	$0.013\pm^{0.002}_{0.002}$	$0.012\pm^{0.003}_{0.003}$
Nickel energy[f]	$7.48\pm^{0.05}_{0.05}$	$7.48\pm^{0.04}_{0.04}$	$7.49\pm^{0.05}_{0.05}$	$7.48\pm^{0.05}_{0.06}$
FeK_α EW[g]	$0.97\pm^{0.35}_{0.29}$	$0.92\pm^{0.25}_{0.20}$	$0.94\pm^{0.17}_{0.24}$	$0.94\pm^{0.34}_{0.32}$
Fe xxv EW[g]	$0.10\pm^{0.10}_{0.02}$	$0.08\pm^{0.09}_{0.02}$	$0.09\pm^{0.09}_{0.02}$	$0.09\pm^{0.09}_{0.02}$
FeK_β EW[g]	$0.14\pm^{0.05}_{0.04}$	$0.12\pm^{0.04}_{0.03}$	$0.15\pm^{0.03}_{0.04}$	$0.15\pm^{0.05}_{0.05}$
Nickel EW[g]	$0.11\pm^{0.05}_{0.04}$	$0.13\pm^{0.04}_{0.04}$	$0.11\pm^{0.04}_{0.04}$	$0.10\pm^{0.05}_{0.04}$
FPMB/FPMA[h]	$0.99\pm^{0.03}_{0.03}$	$1.03\pm^{0.02}_{0.02}$	$1.03\pm^{0.01}_{0.01}$	$1.02\pm^{0.03}_{0.03}$
PHA bins	1054	1206	1251	1064
d.o.f.	1045	1197	1242	1055
χ^2	1070.9	1265.6	1343.8	1117.603
reduced χ^2	1.02	1.06	1.08	1.06
χ^2 probability	28.2%	8.2%	2.3%	8.2%
5–10 keV flux[i]	$1.87\pm^{0.05}_{0.05}$	$2.00\pm^{0.03}_{0.03}$	$2.05\pm^{0.03}_{0.03}$	$2.08\pm^{0.08}_{0.05}$
10–40 keV flux[i]	$61\pm^{4}_{4}$	$86\pm^{5}_{6}$	$121\pm^{6}_{6}$	$154\pm^{9}_{11}$
40–79 keV flux[i]	$76\pm^{4}_{11}$	$102\pm^{4}_{2}$	$135\pm^{2}_{4}$	$175\pm^{5}_{19}$
L(2–10 keV)[l]	12.3	24.8	42.1	54.4
λ_{Edd}	0.07	0.14	0.24	0.32
covering factor	$0.14\pm^{0.26}_{0.14}$	$0.16\pm^{0.06}_{0.04}$	$0.12\pm^{0.03}_{0.03}$	$0.11\pm^{0.04}_{0.04}$

Notes. Best-fit values with uncertainties at the 90% confidence level for one parameter of interest ($\Delta\chi^2 = 2.706$) for states L, M, H, and SH.
[a] Direct power-law photon index.
[b] Column density N_H in units of 10^{24} cm^{-2}.
[c] Normalization at 1 keV of the direct power law in units of photons keV^{-1} cm^{-2} s^{-1}.
[d] Normalization at 1 keV of the forward-reflection component in units of photons keV^{-1} cm^{-2} s^{-1};
[e] Normalization at 1 keV of the back-reflection component in units of photons keV^{-1} cm^{-2} s^{-1}.
[f] Nickel line energy in units of keV.
[g] Line equivalent width in units of keV.
[h] Normalization factor between FPMB and FPMA.
[i] FPMA *NuSTAR* observed flux in units of 10^{-12} erg cm^{-2} s^{-1}.
[l] FPMA *NuSTAR* intrinsic 2–10 keV luminosity in units of 10^{41} erg s^{-1} for D = 3.8 Mpc (Mouhcine et al. 2005; Mould & Sakai 2008; Tully et al. 2008, 2009; Jacobs et al. 2009; Nasonova et al. 2011).

Considering all of the model components, the best-fit values of the normalization factors for the *Suzaku* observations with respect to the first observation are $1.054\pm^{0.08}_{0.07}$, $0.984\pm^{0.08}_{0.08}$, $1.037\pm^{0.08}_{0.08}$, and $1.01\pm^{0.07}_{0.07}$, respectively. The normalization of the first *Suzaku* observation with respect to the 2004 *Chandra* observation is 0.97. The normalization of the 2004 *Chandra* observation with respect to the *NuSTAR* observations is 1.07 ± 0.05. In the final spectral analysis, we only allow variations of the normalization factor of the 2004 *Chandra* observation with respect to the *NuSTAR* spectra; we fix the normalizations of the 2000 *Chandra* and *Suzaku* observations to the ratio between the best-fit values reported above and the 2004 *Chandra* observation one.

5.3. Results

The spectral analysis for the four states (L, M, H, and SH) is performed by jointly fitting the *NuSTAR* (3–79 keV), *Suzaku* XIS (3–7.8 keV), and *Chandra* (0.5–7.8 keV) data, using the five-component spectral model described above. The best-fit

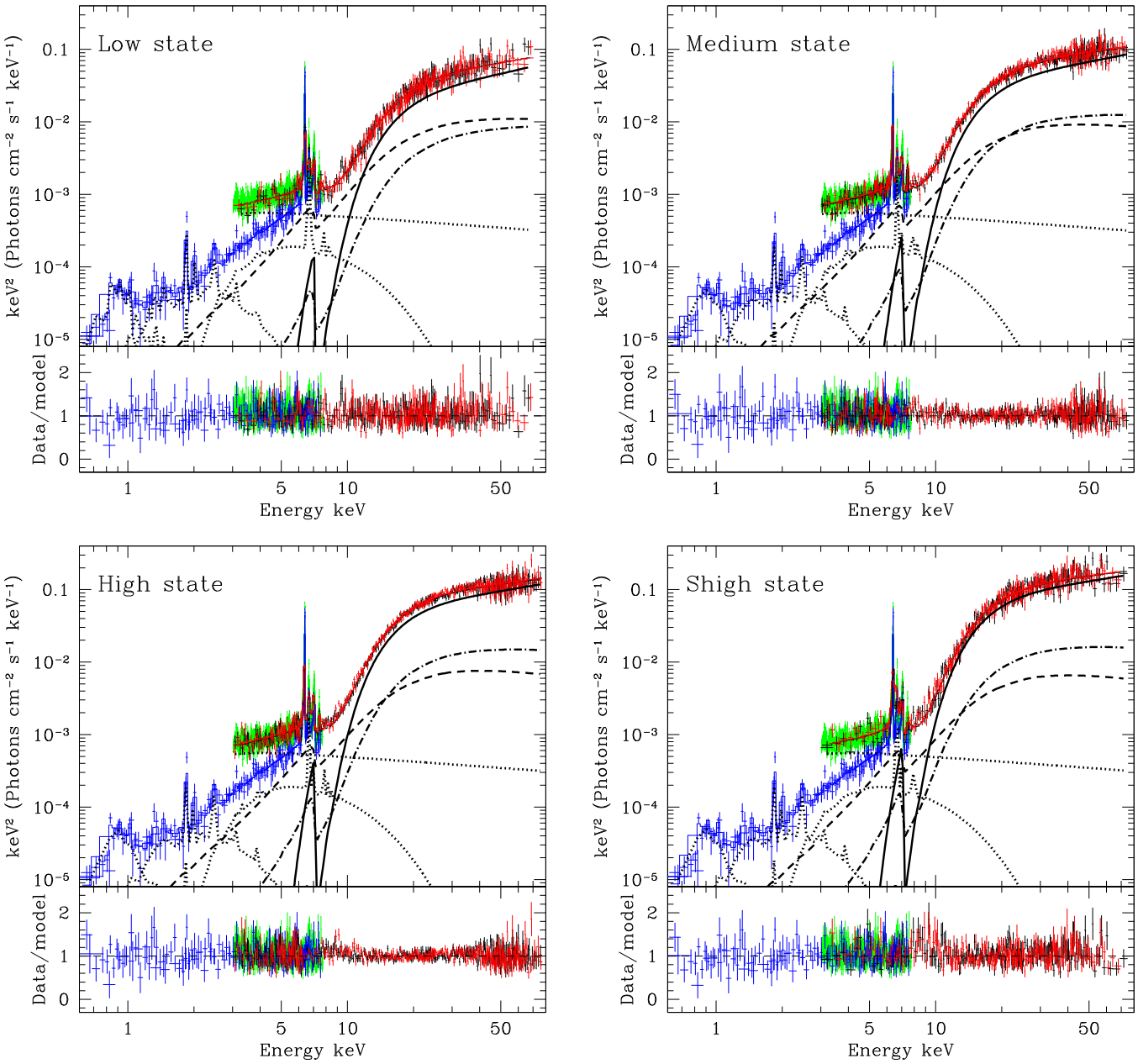

Figure 12. Broadband best-fit spectra, models (upper panels), and residuals (lower panels) for the L, M, H, and SH states (from top to bottom, clockwise). The *NuSTAR* (black is FPMA and red is FPMB), the five *Suzaku* (green) and *Chandra* (blue) spectra unfolded with the instrument responses (for single *Suzaku* and *Chandra* spectra see Figures 9 and 11, respectively) are reported in the upper panels. The total model, including the FeK_α, FeK_β, and nickel lines (not shown as single components for clarity), is superimposed. The model single continuum components are also shown: the primary continuum (black solid lines), the back-reflection (black dashed lines), the forward-reflection (black dashed-dotted lines), the three thermal spectra and the power law due to the contribution of the serendipitous sources in the NGC 4945 field (black dotted lines). In the lower panels, the data/best-fit model ratios are shown.

(A color version of this figure is available in the online journal.)

parameters are reported in Table 6, the broadband best-fit spectra, residuals, and models in the four states are reported in Figure 12 and the confidence contours of the joint errors for different parameters of interest are shown in Figure 13. The nucleus is obscured by Compton-thick matter with a remarkably constant column density $N_{\rm H}$ from the L to the SH state of the order of 3.55×10^{24} cm^{-2}, corresponding to $\tau_{\rm Thomson} \sim 2.9$. The primary continuum spectral slope slightly steepens ($\Delta\Gamma \sim 0.2$) when the source gets brighter (Figure 13, top panel), with a behavior typical of Seyfert galaxies on longer timescales (e.g., Sobolewska & Papadakis 2009; Caballero-Garcia et al. 2012). The primary continuum flux, without considering the contribution of the constant reflected components, in the 10–40 keV energy range increases from the L to the SH state by a factor of ∼3.3. The flux impinging on the Compton-thick obscuring gas and scattered into the line of sight (A_{S90} in Table 6) is correlated with the primary flux, albeit with a much lower variability amplitude (less than a factor of 1.2; see Figure 13, lower panel) as expected due to the smearing effect introduced by scattering in the obscuring gas. The forward-scattered flux becomes progressively less constrained when the intrinsic flux becomes fainter. In the L state it is not formally detected, though the 90% upper limit is consistent with the values in the M, H, and SH states.

The back-reflection component (A_{S0}) is almost constant (within a few tens of percent) across the various states. There

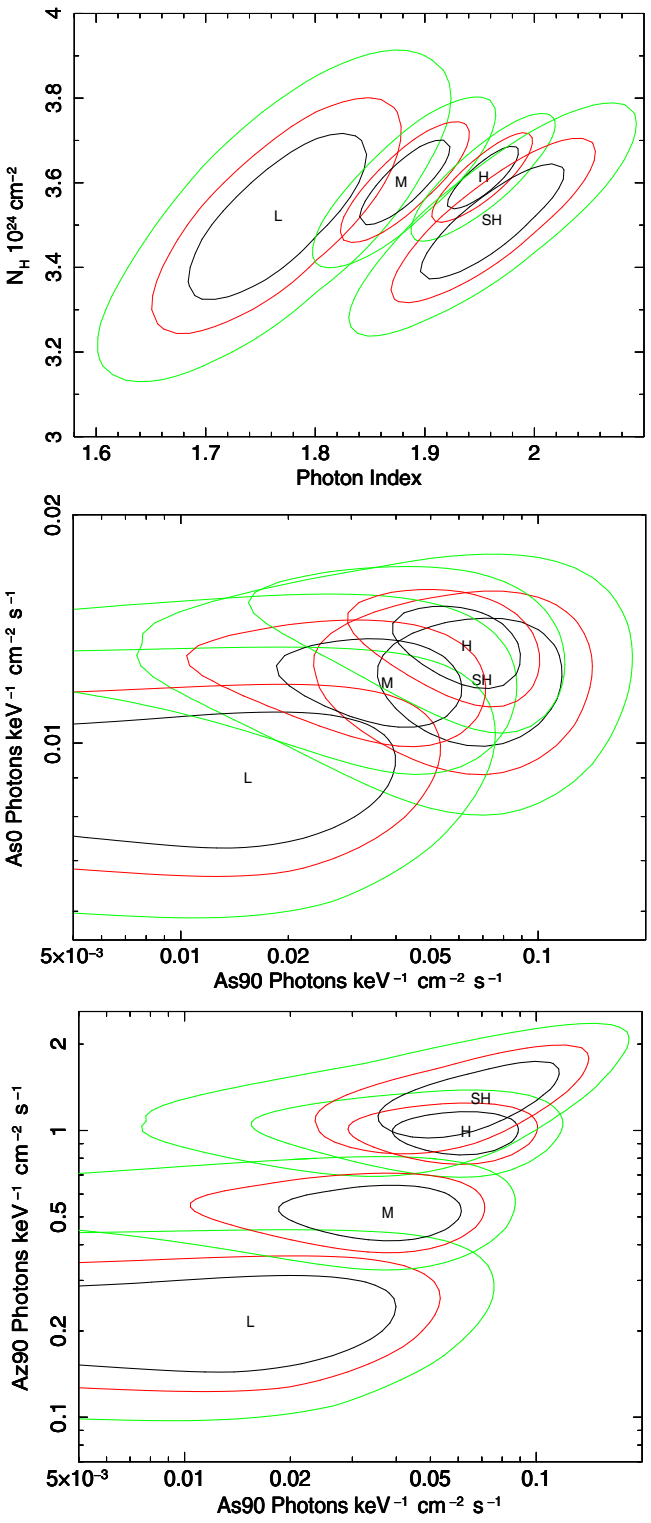

Figure 13. 68%, 90%, and 99% confidence contours for the L, M, H, and SH states for different model parameters. Top panel: column density $N_{\rm H}$ vs. photon index for the direct continuum. Middle panel: normalization of the back-reflected continuum vs. normalization of the forward-scattered continuum. Bottom panel: normalization of the back-reflected continuum vs. the normalization of the direct continuum.

(A color version of this figure is available in the online journal.)

is no clear evidence of a difference in the column density $N_{\rm H}$ between the matter responsible for absorption, scattering, and reflection.

Following Yaqoob (2012), in a time-steady situation, we can estimate a covering factor from A_{S90}/A_{Z90} if $(A_{S90}/A_{Z90}) \ll 1$, as we indeed find. The original geometry assumed in the Monte Carlo calculations to generate the MYTORUS tables (i.e., $A_{S90}/A_{Z90} = 1$) corresponds to a covering factor of 0.5. Therefore, for a different configuration, the covering factor can be obtained by the ratio above rescaled by a factor of 0.5. The best-fit values reported in Table 6 indicate a relatively constant covering factor of ∼0.13.

The observed iron and nickel line intensities are consistent, but much better constrained than previous measurements reported in the literature. There is no evidence of variability in the line equivalent widths and fluxes (evaluated following the method in Section 7.3.5.4 of the MYTORUS manual). The mean values of the line fluxes in units of 10^{-14} erg cm^{-2} s^{-1} are 31.3 ± 0.5, 3.2 ± 0.3, 4.5 ± 0.5, and 2.5 ± 0.9 for the FeK_α, Fe XXV, FeK_β and nickel line, respectively. The highly ionized helium-like iron line is also remarkably constant, suggesting that it may be associated with the hottest component of the multi-temperature plasma.

5.4. Comparison with Standard Reflection Models

For the sake of completeness, and to facilitate comparison with previous results in the literature, we briefly describe the results obtained by fitting a standard torus model and use simpler approximations for the absorption and reflection in Compton-thick media.

Fitting the MYTORUS model in the original geometry (i.e., "coupled" mode, which represents a uniform torus with a half-opening angle of 60° and a 0.5 covering factor) yields significantly worse fits (total $\Delta\chi^2 \sim 800$ with total degrees of freedom decreased by four) with respect to the fits obtained in the "decoupled" mode (see Section 5.3). We can therefore reject this uniform torus model. Leaving the normalization of the forward-scattered component (A_S) free to vary, we obtain statistically good fits. We find that A_S increases from $A_S \sim 0.12 \times A_Z$ for the SH state to $A_S \sim 0.5 \times A_Z$ for the L state; this indicates that the Compton-scattered continuum is much weaker in the H and SH states (as also found by Yaqoob 2012 for the *BeppoSAX* and *Swift* BAT data). These findings provide further evidence against a uniform torus model. Moreover, the L and M states would be reflection-dominated. We can therefore reject this model as inconsistent with the observed variability.

We also considered simpler, but unphysical approximations for the absorption and reflection in Compton-thick media. We modeled the primary continuum transmitted through a high column density absorber with PLCABS (Yaqoob 1997). We modeled the reflection component with an exponentially cut-off power-law spectrum reflected from neutral material with infinite column density using PEXRAV (Magdziarz & Zdziarski 1995). The absorption column density $N_{\rm H}$ is slightly higher ($\sim 4 \times 10^{24}$ cm^{-2}) and fully consistent with literature fits, while the direct continuum is slightly harder ($\Delta\Gamma \sim 0.1$). The observed variability is due to an increase in the direct continuum emission from the L to SH state, similar to the "decoupled" MYTORUS model.

The statistical quality of the best-fit PLCABS/PEXRAV model is equivalent to the best-fit "decoupled" model described earlier, being the PLCABS/PEXRAV model the most similar to the "decoupled" MYTORUS model as underlined by Yaqoob (2012). A disc/slab geometry, with an infinite column density for the material responsible for the Compton-scattered continuum is assumed in the PEXRAV model. The spectral features associ-

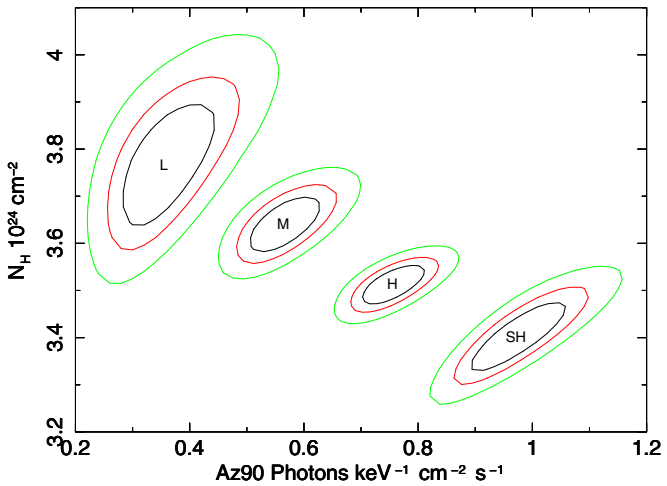

Figure 14. 68%, 90%, and 99% confidence contours for the column density $N_{\rm H}$ vs. the normalization of the direct continuum, for the L, M, H, and SH states. The confidence contours are for the "decoupled" MYTORUS model with the photon index for the direct continuum fixed to 1.9.

(A color version of this figure is available in the online journal.)

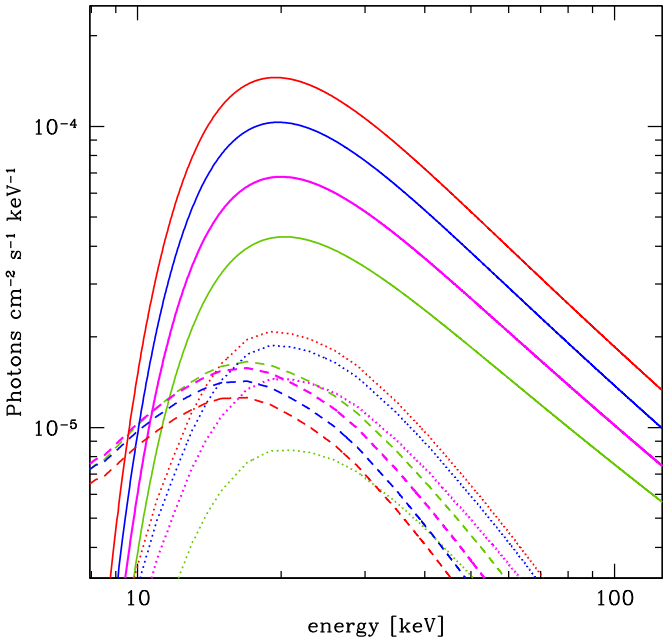

Figure 15. Best-fitting model for the main hard X-ray components: the solid lines represent the direct continuum component, the dotted lines represent the forward-scattered component, and the dashed lines represent the back-reflected continuum component. As in Figure 8, the green, magenta, blue, and red lines represent the L, M, H, and SH states, respectively.

(A color version of this figure is available in the online journal.)

ated with scattering in a finite column density medium cannot be reproduced. Moreover, the column density of NGC 4945 is close to the limit of validity of the PLCABS routines (i.e., $N_H = 5 \times 10^{24}$ cm^{-2}). Finally, as pointed out by Murphy & Yaqoob (2009), using PEXRAV and PLCABS may produce a bias toward solutions dominated by the direct continuum. For all these reasons, MYTORUS returns a more physical description of the observations (Yaqoob & Murphy 2009, 2011, Yaqoob 2012).

5.5. N_H Variability?

The spectral analysis performed with the "decoupled" MYTORUS model suggests changes of the photon index for the primary continuum, and constant column density for the obscuring matter. This behavior could be equivalent to a constant photon index and variable column density. Therefore, to further investigate possible variations of obscuring matter, we performed spectral analysis of the four states L, M, H, and SH using the "decoupled" MYTORUS model with the photon index of the primary continuum fixed to the mean value of $\Gamma = 1.9$. The global quality of the fit worsened (total $\Delta\chi^2 \sim 18$ with total degrees of freedom decreased by four). The best-fit values of the column density of the primary continuum are consistent with being constant ($N_{\rm H} = 3.8 \pm 0.2$, 3.6 ± 0.1, 3.5 ± 0.1, and $3.4 \pm 0.1 \times 10^{24}$ cm^{-2}, for the L, M, H, and SH states, respectively), but show a weak anti-correlation with the primary continuum (see Figure 14). This behavior suggests that possible variations of the column density could be due to small variations in the ionization state of the absorber, following variations in the intensity of ionizing radiation, rather than to variations in the amount of absorbing gas along the line of sight. We remark that the small variation of the absorption column density is obtained under the hypothesis of a constant photon index, and thus should be considered with caution.

6. DISCUSSION

The state-resolved spectral analysis of the three *NuSTAR* observations of the bright Seyfert 2 galaxy NGC 4945 confirms and extends the results obtained by previous observations in the hard X-ray band. The broadband 3–79 keV emission is characterized by two main spectral components. The first is primary continuum emission piercing through a Compton-thick obscuring medium that shows rapid variability, and dominates the $E > 10$ keV spectrum. The second component, which dominates at $E < 10$ keV, results from a combination of different components, all of them relatively constant: (1) a low-energy tail of the back-reflected nuclear spectrum with neutral emission lines, (2) a multi-temperature thermal plasma due to the nuclear starburst and extended super wind, and (3) a summed contribution of individual point-like sources within 75″ of the NGC 4945 nucleus, modeled with a power law and low temperature plasma.

Given the strong dependence of the spectral shape on the 10–40 keV flux, we extracted four states based on the brightness, which we call L, S, H, and SH (see Figure 6), defined to maximize the number of counts and minimize the hardness ratio variation in each interval. We fit the state-resolved spectra with a self-consistent model for transmission, scattering, and reflection of photons in Compton-thick gas (MYTORUS). We assumed a clumpy distribution for the obscuring and reflecting material with an arbitrary effective global covering factor (i.e., the "decoupled" MYTORUS model). The model choice is driven by the observed hard X-ray variability, strongly suggesting a low covering factor of the obscuring matter in NGC 4945 (see, e.g., Madejski et al. 2000; Done et al. 2003; Yaqoob et al. 2012). The state-resolved spectral analysis indicates that in all the states $A_{S90} \ll A_{Z90}$ and $A_{S0} \sim 20\% \times A_{S90}$, which can be interpreted as a patchy absorber with a small covering factor and a large filling factor. This interpretation would be also consistent with the lack of strong column density variations, due to moving clouds. A uniform distribution of obscuring gas (either a standard torus or a edge-on ring) are ruled out by the present observations. The hard X-ray (>8 keV) components for the best-fit model are summarized in Figure 15. It is clear that most of the variability is due to the primary continuum, varying by a factor

of ∼3.3. The forward scattered component is variable, though with a lower amplitude (less than a factor of two), whereas the back-reflected component remains approximately constant within 10%. Qualitatively, the lower fractional variability of the scattered/reflected components is due to the larger path length of the reprocessed photons in the obscuring medium. To roughly estimate the distance of this medium from the nucleus, we followed the method described in Marinucci et al. (2012). The circumnuclear gas is modeled as a cylinder with the axis on the plane of the sky, radius R and height H. We assumed $H/R = 0.13$ (i.e., the covering factor) and we considered a single *NuSTAR* 10–40 keV light curve to determine the maximum observable flux variation of the reflected component as a function of the distance R. The fractional variability in the iron line flux is within ∼5%. The minimum distance needed to smear out the observed hard X-ray variability in the 10–40 keV energy range is $R > 10$ light days. The weakly constrained lower limit on the distance of the reprocessor is due to the short timescales probed by continuous NuSTAR observations. As a comparison, the $R > 35$ pc limit calculated by Marinucci et al. 2012 is obtained from the monitoring of the hard X-ray variability on a much longer time scale (i.e., the 65 month *Swift* BAT monitoring).

From a visual inspection of the broadband best-fit spectra and residuals in the four states (see Figure 12), there is no evidence of a high-energy curvature in the spectrum due to a cutoff in the primary continuum. The quality of the spectra is not sufficient to break the degeneracy between the spectral parameters. Assuming the power-law spectrum within the 90% range of the best-fit for each state, the addition of a high-energy exponential roll-over does not improve the fit and the lower limits (at the 90% confidence level) on the e-folding energy are of the order of 200–300 keV in the L, M, and H states. An exponential cutoff at $E_C = 190^{+200}_{-40}$ keV improves the fit ($\Delta\chi^2 \sim 11$ for 1 degree of freedom) in the SH state. Additional observations would be needed to confirm whether the exponential cutoff is correlated with the source flux. The present values agree fairly well with those previously reported by *BeppoSAX* (∼80–500 keV at the 90% confidence level; Guainazzi et al. 2000), *Suzaku* (>80 keV; Itoh et al. 2008) and *Swift* BAT (>100 keV; Yaqoob 2012).

We compute the 2–10 keV intrinsic luminosity assuming the best-fit parameters and correcting for the intrinsic absorption. The bolometric luminosities in the L, M, H, and SH states are calculated assuming the bolometric corrections for type 2 AGN of Lusso et al. (2011). In the range of the observed X-ray luminosities (∼1.2–5.4 × 10^{42} erg s^{-1}) the bolometric corrections are of the order of 10 with a small dispersion. The inferred accretion rate $\lambda_{\rm Edd} = L_{\rm bol}/L_{\rm Edd}$, assuming a black hole mass of 1.4 × 10^6 $M_\odot$, is ∼0.07, 0.14, 0.24, and 0.32 for the L, M, S, and SH states, respectively. These values are significantly smaller than those reported by Yaqoob (2012) from the analysis of a large set of archival observations. We note that Yaqoob (2012) assumed a distance of about 8 Mpc (see his Tables 4 and 5), which is ∼ twice that adopted in this paper; this explains the discrepancy in the accretion rate estimates.

At face value, the accretion rate in the four different states correlates with the intrinsic continuum spectral slope (Figure 16). However, this relation is obtained with the assumption that the X-ray luminosity variability traces the bolometric one in lock-step and with the same fractional degree of variability. This assumption may not necessarily be true and it is known that variability timescales are usually longer in the UV than in the X-rays (i.e., Maoz et al. 2002; Nandra et al. 2000; Clavel et al. 1992).

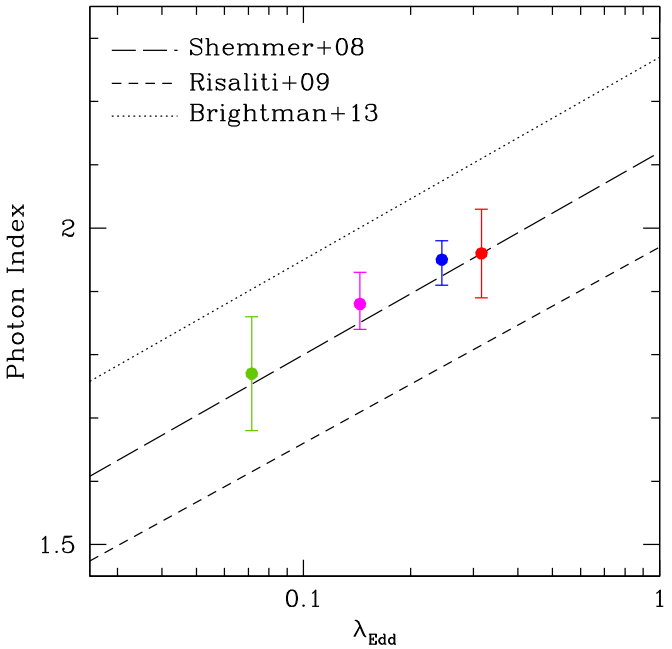

Figure 16. Photon index vs. the Eddington ratio for the L (green), M (magenta), H (blue) and SH (red) states. The long dashed, short dashed, and dotted lines indicate the analytical fit found by Shemmer et al. (2008), Risaliti et al. (2009), and Brightman et al. (2013), respectively.

(A color version of this figure is available in the online journal.)

Even if the slope of the relation and its normalization are close to that of a few AGN type 1 samples for which the accretion rate could be measured (Shemmer et al. 2008; Risaliti et al. 2009; Brightman et al. 2013), we caution about the use of single-epoch X-ray data to derive $\lambda_{\rm Edd}$ values for obscured AGN in the distant universe.

The most remarkable and unique characteristic of the NGC 4945 hard (>10 keV) X-ray emission is the large amplitude and fast variability of the primary continuum piercing through a constant column density Compton-thick absorber. In Figure 17, we reported the history of hard X-ray variability from *BeppoSAX* PDS, *Swift* BAT, *Suzaku* PIN, and *NuSTAR* data. The observed count rates are converted to the 15–80 keV X-ray flux assuming the average best-fit values from the *NuSTAR* spectra ($\Gamma = 1.9$ and $N_H = 3.55 \times 10^{24}$ cm^{-2}). The unprecedented statistical quality of the *NuSTAR* observations is evident from a visual inspection of the panel. With the possible exception of *BeppoSAX* PDS, the amplitude variability is similar among the various observations and fully sampled by *NuSTAR* data. The observed range of accretion rates is thus likely to be representative of the nuclear accretion history over the last ∼15 years.

The nucleus of NGC 4945 is accreting at a rate that is faster (∼0.1–0.3) than the typical values $\lambda_{\rm Edd} < 0.1$ of obscured Seyfert 2 galaxies in the local universe (Vasudevan et al. 2010). The possibility of episodes of super Eddington accretion over the past ∼15 years, are ruled out by the present analysis. Even though not as extreme as previously claimed, the typical accretion rate of NGC 4945 lies on the extreme of the distribution observed for Seyfert 2 galaxies and is more typical of a luminous QSO.

The low covering factor of the Compton-thick obscuring gas, as inferred for the first time on a sound statistical footing via state-resolved spectral analysis, and the high accretion rate

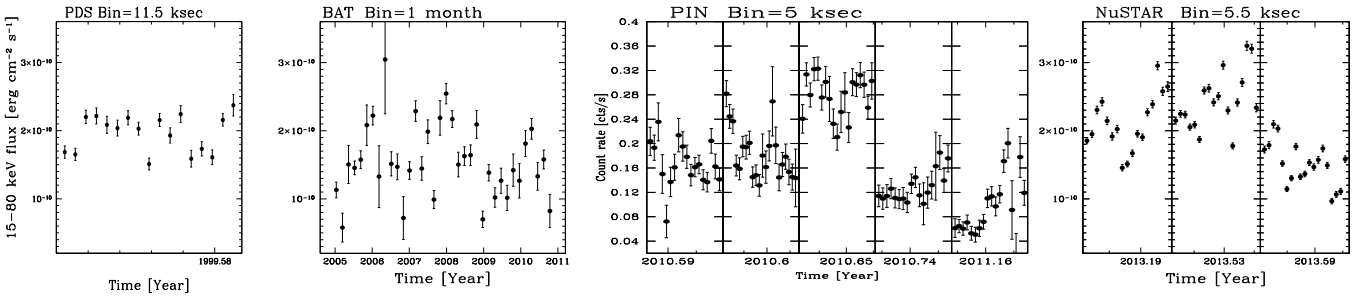

Figure 17. From right to left: the *BeppoSAX* PDS, *Swift* BAT, *Suzaku* HXD PIN, and 15–79 keV *NuSTAR* background-subtracted light curves in bins of 11.5 ks, 1 month, 5 ks and 5.5 ks, respectively. The observed count rates are converted to the 15–80 keV X-ray flux assuming the average best-fit values from the *NuSTAR* spectra (see Section 6).

make NGC 4945 an extremely interesting source. The observed properties are typical of the AGN population postulated in the synthesis models for the X-ray background to fit the 20–30 keV peak and expected to be abundant at $z \simeq 1$–2. Further X-ray monitoring of this "Rosetta Stone" would further constrain the geometry and the physics of the most obscured, rapidly accreting black holes. More specifically, a dense monitoring would allow a finer analysis of the state-resolved spectral analysis. Moreover, long term variability would place stronger constraints on the distribution of the absorbing material.

7. CONCLUSION

We present the *NuSTAR* spectra of NGC 4945, one of the brightest Seyfert 2 galaxies in the local universe. Three *NuSTAR* observations obtained over a time interval of about five months provide spectra and variability of unprecedented quality, allowing detailed modeling of the source geometry. The primary findings can be summarized as follows.

1. In the *NuSTAR* band, the source is highly variable with a doubling/halving time as short as 16 ks. The maximum variability is in the 10–40 keV band, while below 10 keV the source is constant.
2. The analysis of the hardness ratio light curves implies strong spectral variability above 8–10 keV, which has been addressed for the first time in this source, via state-resolved spectral analysis of the *NuSTAR* high-energy spectra.
3. The state-resolved spectral analysis, confirmed that the constant X-ray flux below 10 keV is consistent with being due to reflection from Compton-thick material. The shape of the reflected continuum below 10 keV and the iron line complex has been determined by combining *NuSTAR* with *Suzaku* and *Chandra* observations.
4. The variability in the hard X-ray (>10 keV) band is mainly due to variation in the intensity of the primary continuum piercing through a high column density $N_{\rm H} \sim 3.6 \times 10^{24}$ cm^{-2} absorber. There is evidence of a steepening of the primary continuum spectral slope with increasing flux. The spectral and variability properties indicate, in agreement with previous results, a small covering factor (∼0.1–0.15) for the obscuring matter, which is best parameterized in terms of a clumpy toroidal distribution.
5. A power spectral density analysis suggests that the variability is almost identical to that observed in Seyfert 1 galaxies, reinforcing the interpretation of spectral variability as being due to variations in the primary emission.
6. There is no clear evidence for a high-energy cut-off with lower limits of the order of ∼200–300 keV.
7. The intrinsic continuum variability is associated with a variation of the Eddington ratio in the range of 0.1–0.3. Assuming a distance of ∼3.8 Mpc, there is no evidence of super Eddington accretion.
8. With the assumption that the X-ray luminosity variations trace the bolometric luminosity, the accretion rate correlates with the intrinsic spectral index, in agreement with the trend observed for relatively high-redshift AGNs. The fact that the same trend is observed for different states of the same source lend further support to a close link between the hard X-ray slope and the physics of accretion processes.

This work was supported under NASA Contract NNG08FD60C and made use of data from the *NuSTAR* mission, a project led by the California Institute of Technology, managed by the Jet Propulsion Laboratory, and funded by the National Aeronautics and Space Administration. We thank the *NuSTAR* Operations, Software, and Calibration teams for support with the execution and analysis of these observations. This research has made use of the *NuSTAR* Data Analysis Software (NuSTARDAS) jointly developed by the ASI Science Data Center (ASDC, Italy) and the California Institute of Technology (USA). S.P., A.C., F.F., and G.M. acknowledge support from the ASI/INAF grant I/037/12/0–011/13. A.C. acknowledges the Caltech Kingsley visitor program. P.G. acknowledges support from STFC (grant reference ST/J003697/1). G.B.L. acknowledges support from STFC (grant reference ST/K501979/1). D.M.A. acknowledges support from STFC (grant reference ST/I001573/1) and from the Leverhulme Trust. P.A. acknowledges financial support from Fondecyt grant 11100449 and Anillo ACT1101. G.R. acknowledges financial support from grant NASA GO3–14109X. M.K. gratefully acknowledges support from Swiss National Science Foundation Grant PP00P2_138979/1. W.N.B. and B.L. acknowledge support from California Institute of Technology NuSTAR subcontract 44A–1092750 and NASA ADP Grant NNX10AC99G. F.E.B. acknowledges support from Basal–CATA PFB–06/2007, CONICYT–Chile (grants FONDECYT 1101024 and "EMBIGGEN" Anillo ACT1101), and Project IC120009 "Millennium Institute of Astrophysics (MAS)" of Iniciativa Científica Milenio del Ministerio de Economía, Fomento y Turismo. S.P. is grateful to Tahir Yaqoob for useful discussions on the MYTORUS model.

REFERENCES

Arévalo, P., Churazov, E., Zhuravleva, I., Hernndez-Monteagudo, C., & Revnivtsev, M. 2012, MNRAS, 426, 1793

Arnaud, K. A. 1996, in ASP Conf. Ser. 101, Astronomical Data Analysis Software and Systems V, ed. G. H. Jacoby & J. Barnes (San Francisco, CA: ASP), 17
Baumgartner, W. H., Tueller, J., Markwardt, C. B., et al. 2013, ApJS, 207, 19
Bianchi, S., Guainazzi, M., & Chiaberge, M. 2006, A&A, 448, 499
Boldt, E. 1987, PhR, 146, 215
Boller, Th., Keil, R., Hasinger, G., et al. 2003, A&A, 411, 63
Brandt, W. N., Iwasawa, K., & Reynolds, C. S. 1996, MNRAS, 281L, 41
Brenneman, L. W., Madejski, G., Fuerst, F., et al. 2014, ApJ, 788, 61
Brightman, M., Silverman, J. D., Mainieri, V., et al. 2013, MNRAS, 433, 2485
Caballero-Garcia, M. D., Papadakis, I. E., Nicastro, F., & Ajello, M. 2012, A&A, 537A, 87
Clavel, J., Nandra, K., Makino, F., et al. 1992, ApJ, 393, 113
Done, C., Madejski, G. M., & Smith, D. A. 1996, ApJL, 463, L63
Done, C., Madejski, G. M., Zycki, P. T., & Greenhill, L. J. 2003, ApJ, 588, 763
Dos Santos, P. M., & Lepine, J. R. D. 1979, Natur, 278, 34
Fiore, F., Guainazzi, M., & Grandi, P. 1999, http://heasarc.nasa.gov/docs/sax/abc/saxabc/saxabc.html
Frontera, F., Costa, E., dal Fiume, D., et al. 1997, Proc. SPIE, 3114, 206
Fruscione, A., McDowell, J. C., Allen, G. E., et al. 2006, Proc. SPIE, 6270E, IV
Gehrels, N., Chincarini, G., Giommi, P., et al. 2004, ApJ, 611, 1005
Gilli, R., Comastri, A., & Hasinger, G. 2007, A&A, 463, 79
Greenhill, L. J., Moran, J. M., & Herrnstein, J. R. 1997, ApJL, 481, L23
Gruber, D. E., Matteson, J. L., Peterson, L. E., & Jung, G. V. 1999, ApJ, 520, 124
Guainazzi, M., & Bianchi, S. 2007, MNRAS, 374, 1290
Guainazzi, M., Matt, G., Brandt, W. N., et al. 2000, A&A, 356, 463
Harrison, F. A., Craig, W. W., Christensen, F. E., et al. 2013, ApJ, 770, 103
Heiles, C., & Cleary, M. N. 1979, AuJPA, 47, 1
Isobe, N., Kubota, A., Makishima, K., et al. 2008, PASJ, 60S, 241
Itoh, T., Done, C., Makishima, K., et al. 2008, PASJ, 60, S251
Iwasawa, K., Koyama, K., Awaki, H., et al. 1993, ApJ, 409, 155
Jacobs, B. A., Rizzi, L., Tully, R. B., et al. 2009, AJ, 138, 332
Kokubun, M., Makishima, K., Takahashi, T., et al. 2007, PASJ, 59S, 53
Lusso, E., Comastri, A., Vignali, C., et al. 2011, A&A, 534A, 110
Madejski, G., Zycki, P., Done, C., et al. 2000, ApJ, 535L, 87
Magdziarz, P., & Zdziarski, A. A. 1995, MNRAS, 273, 837
Maoz, D., Markowitz, A., Edelson, R., & Nandra, K. 2002, AJ, 124, 1988
Marinucci, A., Risaliti, G., Wang, Junfeng., et al. 2012, MNRAS, 423L, 6
Matt, G., Brandt, W. N., & Fabian, A. C. 1996, MNRAS, 280, 823
McHardy, I. M., Koerding, E., Knigge, C., Uttley, P., & Fender, R. P. 2006, Natur, 444, 730
Mouhcine, M., Ferguson, H. C., Rich, R. M., Brown, T. M., & Smith, T. E. 2005, ApJ, 633, 810
Mould, J., & Sakai, S. 2008, ApJL, 686, L75
Mueller, M., Madejski, G., Done, C., & Zycki, P. 2004, in AIP Conf. Ser. 714, X-Ray Timing 2003: Rossi and Beyond, ed. P. Kaaret, F. K. Lamb, & J. H. Swank (Melville, NY: AIP), 190
Murphy, K. D., & Yaqoob, T. 2009, MNRAS, 397, 1549
Nandra, K., Le, T., George, I. M., Edelson, R. A., et al. 2000, ApJ, 544, 734
Nasonova, O. G., de Freitas Pacheco, J. A., & Karachentsev, I. D. 2011, A&A, 532A, 104
Ott, M., Whiteoak, J. B., Henkel, C., & Wielebinski, R. 2001, A&A, 372, 463
Perri, M. S., Puccetti, N., Spagnuolo,, et al. 2013, http://heasarc.gsfc.nasa.gov/docs/nustar/analysis/nustardas_swguide_pdf
Pietsch, W., Roberts, T. P., Sako, M., et al. 2001, A&A, 365L, 174
Risaliti, G., Young, M., & Elvis, M. 2009, ApJL, 700, L6
Schurch, N. J., Roberts, T. P., & Warwick, R. S. 2002, MNRAS, 335, 241
Shemmer, O., Brandt, W. N., Netzer, H., Maiolino, R., & Kaspi, S. 2008, ApJ, 682, 81
Sobolewska, M. A., & Papadakis, I. E. 2009, MNRAS, 399, 1597
Swartz, D. A., Ghosh, K. K., Tennant, A. F., & Wu, K. 2004, ApJS, 154, 519
Treister, E., Urry, C. M., & Virani, S. 2009, ApJ, 696, 110
Tully, R. B., Rizzi, L., Shaya, E. J., et al. 2009, AJ, 138, 323
Tully, R. B., Shaya, E. J., Karachentsev, I. D., et al. 2008, ApJ, 676, 184
Vasudevan, R. V., Fabian, A. C., Gandhi, P., Winter, L. M., & Mushotzky, R. F. 2010, MNRAS, 402, 1081
Walton, D. J., Harrison, F. A., Grefenstette, B. W., et al. 2014, ApJ, 793, 21
Walton, D. J., Roberts, T. P., Mateos, S., & Heard, V. 2011, MNRAS, 416, 1844
Yaqoob, T. 1997, ApJ, 479, 184
Yaqoob, T. 2012, MNRAS, 423, 3360
Yaqoob, T., & Murphy, K. D. 2011, MNRAS, 412, 1765